



Provided by the author(s) and University of Galway in accordance with publisher policies. Please cite the published version when available.

Title	An actuatable soft reservoir modulates host foreign body response
Author(s)	Dolan, Eimear B.; Varela, C. E.; Mendez, K.; Whyte, W.; Levey, R. E.; Robinson, S. T.; Maye, E.; O'Dwyer, J.; Beatty, R.; Rothman, A.; Fan, Y.; Hochstein, J.; Rothenbacher, S. E.; Wylie, R.; Starr, J. R.; Monaghan, M.; Dockery, P.; Duffy, G. P.; Roche, E. T.
Publication Date	2019-08-28
Publication Information	Dolan, E. B., Varela, C. E., Mendez, K., Whyte, W., Levey, R. E., Robinson, S. T., Maye, E., O'Dwyer, J., Beatty, R., Rothman, A., Fan, Y., Hochstein, J., Rothenbacher, S. E., Wylie, R., Starr, J. R., Monaghan, M., Dockery, P., Duffy, G. P., Roche, E. T. (2019). An actuatable soft reservoir modulates host foreign body response. <i>Science Robotics</i> , 4(33), eaax7043. doi: 10.1126/scirobotics.aax7043
Publisher	American Association for the Advancement of Science
Link to publisher's version	https://dx.doi.org/10.1126/scirobotics.aax7043
Item record	http://hdl.handle.net/10379/15845
DOI	http://dx.doi.org/10.1126/scirobotics.aax7043

Downloaded 2024-04-26T05:50:17Z

Some rights reserved. For more information, please see the item record link above.



Title: An actuatable soft reservoir modulates host foreign body response

Short Title: Dynamic reservoir modifies host response

Authors

E.B. Dolan^{1,2,3}, C.E. Varela^{1,4}, K. Mendez^{1,4}, W. Whyte^{1,3,5,6}, R.E. Levey³, S.T. Robinson^{3,6}, E. Maye³, J. O'Dwyer^{2,3}, R. Beatty³, A. Rothman⁷, Y. Fan⁷, J. Hochstein⁷, S.E. Rothenbucher¹, R. Wylie³, J.R. Starr⁸, M. Monaghan^{5,9}, P. Dockery^{3,10}, *G.P. Duffy^{3,5,6,10}, *E.T Roche^{1,7}.

Affiliations

1. Institute for Medical Engineering and Science, Massachusetts Institute of Technology, Cambridge, MA, USA
2. Biomedical Engineering, College of Engineering and Informatics, National University of Ireland, Galway, Ireland
3. Anatomy & Regenerative Medicine Institute (REMEDI), School of Medicine, College of Medicine Nursing and Health Sciences, National University of Ireland Galway, Ireland
4. Harvard-MIT Program in Health Sciences and Technology, Cambridge, MA, USA
5. Trinity Centre for Bioengineering, Trinity Biomedical Sciences Institute, Trinity College Dublin, Dublin 2, Ireland
6. Advanced Materials and BioEngineering Research Centre (AMBER), Trinity College Dublin, Royal College of Surgeons Ireland, & National University of Ireland Galway, Ireland
7. Department of Mechanical Engineering, Massachusetts Institute of Technology, Cambridge, MA, USA
8. Epidemiology and Biostatistics Core, The Forsyth Institute, 245 First Street, Cambridge, MA, USA
9. Department of Mechanical and Manufacturing Engineering, School of Engineering, Trinity College Dublin, Dublin 2, Ireland
10. CÚRAM, Centre for Research in Medical Devices, National University of Ireland Galway, Galway, Ireland.

*These authors jointly supervised this work and are both corresponding authors

Corresponding Authors

Prof. Garry Duffy, Anatomy, School of Medicine, College of Medicine Nursing and Health Sciences, National University of Ireland Galway, Ireland. email: garry.duffy@nuigalway.ie

Prof. Ellen Roche, Institute for Medical Engineering and Science and Department of Mechanical Engineering, Massachusetts Institute of Technology, Cambridge, MA, USA. email: etr@mit.edu

Abstract

The performance of indwelling medical devices that depend on an interface with soft tissue is plagued by complex, unpredictable foreign body responses. Such devices, including breast implants, biosensors, and drug delivery devices are often subject to a collection of biological host responses, including fibrosis, which can impair device functionality. This work describes a milliscale dynamic soft reservoir (DSR) that actively modulates the biomechanics of the biotic-abiotic interface by altering strain, fluid flow and cellular activity in the peri-implant tissue. We performed cyclical actuation of the DSR in a preclinical rodent model. Evaluation of the resulting host response showed a significant reduction in fibrous capsule thickness ($p=0.0005$) in the actuated DSR compared to non-actuated controls, while the collagen density and orientation were not changed. We also show a significant reduction in myofibroblasts ($p=0.0036$) in the actuated group and propose that actuation mediated strain reduces differentiation and proliferation of myofibroblasts and therefore ECM production. Computational models quantified the effect of actuation on the reservoir and surrounding fluid. By adding a porous membrane and a therapy reservoir to the DSR, we demonstrated that with actuation, we can (i) increase transport of a therapy analog and (ii) enhance pharmacokinetics and time to functional effect of an inotropic agent. The soft robotic reservoirs presented here could act as a versatile tool to further understanding, and ultimately to ameliorate, the host response to implantable biomaterials.

Summary: The foreign body response is modulated by a dynamic soft reservoir by altering the biomechanics of the peri-implant tissue

MAIN TEXT

Introduction

The long-term performance of implantable medical devices is drastically limited by complex and unpredictable foreign body responses (FBR). Medical devices that depend on an interface with native tissue are particularly vulnerable, such as neural probes (1, 2), indwelling catheters (3), mammary implants (4), pacemakers (5), glucose biosensors (6-8) and drug and cell delivery devices (6, 9-12). Such devices are often subject to a collection of biological host responses such as fibrosis and inflammation, which can impair functionality. At present, device failure is expected and inevitable, and the costs, inconvenience and morbidity that device failure can impose on patients are largely accepted. The implantable medical devices market is mature and growing (compound annual growth rate of 8%), with an estimated worth of approximately 100 billion US dollars in 2019 (13). Implantable medical devices have various failure rates that can be attributed to fibrosis, and can be as high as 30–50% for implantable pacemakers (5) and 30% for mammoplasty prosthetics (4). Based on a conservative rate of failure due to FBR of 10% for all implantable devices, the value of addressing this critical clinical need is 10 billion per annum.

Once a device is implanted a complex series of events is initiated to protect the host from the ‘foreign body’. Shortly after implantation, fibrinogen and other proteins bind to the surface of the device/foreign body, macrophages then bind and, over time, become multinucleated giant cells releasing inflammatory cytokines. In response to these signals, quiescent fibroblasts are transformed into myofibroblasts, which synthesize procollagen. The procollagen becomes cross-linked and this mature cross-linked collagen and other extracellular matrix proteins contribute to the formation of a dense fibrous capsule that becomes impermeable or hypo-permeable to many compounds (14-17). This dense fibrous capsule can impair the function of implanted devices by obstructing diffusion (drug/cell delivery devices and biosensors) or causing capsular contracture (breast implants). Various strategies have been investigated to mitigate the FBR, such as generating scaffolds that release small molecules (18-21), surface chemistry modifications (22, 23), and modifying implant size and geometry (24-26). However, these treatments have met with limited success because of difficulty in incorporating these modifications in a range of implantable devices.

There is a close relationship between macrophages and myofibroblasts during the fibrotic response and both macrophages and myofibroblasts have been shown to be downregulated when the fibrotic response to implanted alginate spheres is minimized (25, 27). Macrophages have been shown to be a key driver of this downregulated fibrotic response – depletion of the macrophage population resulted in a decreased fibrotic response (25, 27). Strain, fluid agitation and shear stress have been shown to influence the adhesion and proliferation of cells *in vitro* (28-33). Targeting cell activity with altered strain and fluid flow represents an innovative approach to modulate the FBR. Interestingly, we have shown in a previous study that extrinsic magnetic actuation of biphasic ferrogel scaffolds implanted in the proximity of injured muscle reduced fibrous capsule formation around the implant (34).

Soft robotic technologies are highly suited to medical applications involving human interaction due to their inherent conformability and ability to achieve biomimetic motion (35). Implantable soft robots represent a relatively unexplored frontier. Such devices can be implanted in the body for an extended period of time and interact mechanically with tissues to regulate biological function. We have previously reported soft robotic cardiac assist devices that incorporate biomimetic actuation to emulate cardiac function in order to augment ventricular function in the failing heart (36-38). Here we present a milliscale dynamic soft reservoir (DSR) which employs mechanical oscillation to modulate the biomechanics of the biotic-abiotic interface by perturbing fluid flow and cellular activity in the peri-implant tissue. We propose that this motion interferes with the progression of the FBR, and endeavor to characterize this perturbation with *in vitro* and *in vivo* studies. Although we show one design of the DSR in this work, it represents a highly versatile and tunable dynamic platform that can be integrated into implantable devices to improve clinical

outcomes, or tuned as a research tool to further elucidate mechanisms of the fibrotic response to implanted materials.

Results

Realization of Dynamic Soft Reservoir (DSR)

In this work we introduce an implantable pneumatically actuatable reservoir. The device can be cyclically actuated by an implantable pump, and we demonstrate this in a rat model (Fig. 1a, Supplementary Fig. S1 and Supplementary Movie S1). Cyclical pressurization results in a predictable, regime-specific deflection and strain of the lower functional membrane (Fig. 1b, c). Multiple such reservoirs can be incorporated into a thin, conformable matrix that can be designed to be part of, or surround, implantable devices to reduce the host FBR (Supplementary Fig. S2). The proposed mechanism of action of the individual reservoirs is shown in Fig. 1b and c. When the actuation reservoir is pressurized through the actuation line, the volume, and then pressure of the chamber increases. This causes a downward deflection of the middle, and subsequently the lower membrane. Actuation causes deflection and strain of the membrane, and results in fluid flow at the tissue interface (blue arrows Fig. 1b and c) which is proposed to interfere with cell activity and initiation of the fibrotic response. We propose two configurations of this device – one version with an impermeable, non-porous lower membrane (Fig. 1b), which would be incorporated in a sheath as a surface modification (suited toward implants with a structural role), and a second version with a permeable, porous membrane (Fig. 1c) that incorporates an additional therapy delivery line to the lower reservoir to allow transport of therapy into the tissue (suited for drug delivery or biosensing applications). The model DSR described in this work has a hemispherical shape (Fig. 2), with a 35 μL therapy reservoir, the size and shape of which was optimized for the delivery of cell-loaded biomaterials to the epicardial surface of the heart, as previously described (39). However, both the size and shape of the DSR can be easily altered by modifying the positive and negative 3D printed molds as shown in Supplementary Fig. S3. For example, a flat configuration of the DSR could be beneficial, and could achieve the same deflection, see Supplementary Movie S2. An analytical model of this membrane deflection for a range of geometries is included in Supplementary Fig. S4.

Computational and experimental characterization of DSR

Pneumatic pressurization of the DSR alters its geometry, and the resulting deflection of the functional membrane causes localized changes to the mechanical environment and perturbations in the fluid flow in proximity to the device. In order to demonstrate this, and to characterize the spatially varying stress and strain in the device, we conducted experimental materials characterization and computational modeling (Fig. 3). First, device materials were characterized. The thermoplastic polyurethane used for the membrane (porous and non-porous) was tensile tested according to ASTM D638. The resulting stress vs strain plots are shown in Fig. 3a. The data was fitted to a hyperelastic material model with the Ogden model being selected as the best fit (Fig. 3b, Supplementary Fig. S4). With this material model as an input, a finite element analysis model was created to demonstrate the overall strain (Fig. 3c), and resulting stress (Fig. 3d) in the inner and outer reservoirs and membrane. This was repeated for the non-porous and porous membranes with maximum in-plane strain of 6.4% and 8.6% respectively (Supplementary Fig. S4). To validate the computational models, we measured the force that the membrane applies to interfacing tissue, using a custom acrylic holder (Supplementary Fig. S4) to consistently support the device in a materials tester, with the functional membrane in contact with the upper load cell. The cyclical forces for two regimes (regime 1 = 1 psi at 1 Hz, regime 2 = 2 psi at 1 Hz) were recorded, and peak forces were compared to each other, and their corresponding FEA models, showing an excellent match between measured and predicted values (Fig. 3e). To further characterize the possible range of input pressures, higher pressures and corresponding forces were also modeled computationally and experimentally (Fig. 3f). A one way ANOVA was performed with *post hoc* Tukey's test to compare the burst pressure of the devices after they were subjected to 100,000 cycles at pressures of regime 1 or regime 2. There was no statistical difference between regime 1 ($p=0.7685$) or regime 2

($p=0.6251$) compared to the non-actuated control (Fig. 3g), indicating that the applied actuation regimes fall within the fatigue limit of the devices. We used a smooth particle hydrodynamics model to quantify the fluid perturbations from device actuations during device actuation in fluid (Fig. 3h), and an analytical model of a hinged plate to assess the sensitivity of the membrane deflection to design and actuation parameters (Supplementary Fig. S5, S6). This study showed that pressure loading and radius size are both positively correlated to the deflection while material stiffness and membrane thickness are negatively correlated to the deflection. Similar correlations are observed for the maximum radial strain and tangential strain (Supplementary Fig. S6). Although pressure loading is positively correlated with deflection in these analytical models, the differences in deflection between the pressures that we investigated *in vitro* and *in vivo* (1 and 2 psi for regime 1 and 2 respectively) are minor (~1% difference in strain and ~0.1 mm difference in deflection, Supplementary Fig. S6).

To investigate the effect of actuation *in vitro*, we seeded the myofibroblasts cell line WPMY-1 on the tissue-interfacing membrane of non-porous DSRs. DSRs were actuated (1 or 2 psi at 1 Hz for 5 mins every 12 hrs) for 14 days and metabolic activity, cell viability and soluble collagen production were compared to non-actuated controls. There was no significant difference between the two actuation regimes (1 and 2) and for this and subsequent *in vivo* studies, we collapsed the variable, and focused on analyzing the difference between control and actuated groups. We found that actuation did not significantly affect cell metabolic activity or viability compared to the non-actuated control and each time-point (Supplementary Fig. S7a-c). We show a downward trend in collagen production normalized by number of cells when comparing actuated to the controls (Supplementary Fig. S7d).

In vivo implantation of non-porous DSR reduces the foreign body response

To evaluate feasibility of the DSR to reduce the FBR *in vivo*, we first demonstrated that actuation forces were achievable with an implantable pump (Fig. 1a and Supplementary Fig. S1). Next, we implanted the non-porous DSR subcutaneously in a rat model (Supplementary Fig. S8) and we subjected the DSR to the actuation regime (Fig. 4a, Supplementary Movie S3) using a custom built external control box (36, 38).

On day 14 the devices were explanted *en bloc* with surrounding tissue and stained with phosphomolybdic acid (PMA) to enable visualization of collagen dense tissues. Images of the device and surrounding soft tissue were acquired using Scanco Medical MicroCT 100. MIMICs (Materialise) software was used for segmentation of the device space (Fig. 4b shown in blue) and the fibrotic capsule present on the membrane of the device (Fig. 4b shown in purple). Volumetric reconstructions of the fibrotic capsule were generated, and a thickness analysis was performed to identify mean capsule thickness. A significant reduction in the mean fibrotic capsule thickness was seen when the device was actuated compared to the control (*** $p = 0.0005$, Fig. 4c,d) and thickness dot plots of each animal are shown in Fig. 4e.

To characterize the effect of actuation on the cellular constituents involved in the FBR, devices explanted on day 14 were sectioned for histological analysis. Collagen fibers are characteristically birefringent which is enhanced with picrosirius staining. Polarized light microscopy was used to assess the quality and organization of the resulting fibrous capsule after staining. Quantification of birefringent fibers, using color threshold segmentation for mature fibers (red/orange) and immature fibers (green), yielded no statistically significant difference between groups ($p>0.05$), irrespective of polarization color (Fig. 5a,b) with an unpaired Students t-test. Quantification of the directional uniformity (coherency) of the collagen fibers showed no statistically significant difference in the fraction of fibers (>0.05 , Fig. 5c) with an unpaired Students t-test, suggesting actuation did not result in a compositional change in the collagen within the fibrous capsule.

Tissue sections were stained with CD68, a pan-macrophage marker, to assess impact of actuation on the macrophage response at the tissue-device interface. Immunofluorescent images (Fig. 5d) were acquired for the control and actuated devices and a stereological approach was

utilized to provide a quantitative analysis of macrophage number (40-42). Numerical density was calculated (Fig. 5e) and refers to the number of, in this case macrophages, within a unit volume of tissue. A paired Students t-test was carried out with no statistically significant difference observed between groups ($p=0.6963$), suggesting that actuation does not influence macrophage number at the device surface.

Immunofluorescent staining was also performed on the tissue sections for alpha smooth muscle actin (α SMA), to assess for the presence of myofibroblasts around the control and actuated DSR (Fig. 5f). An unpaired Students t-test showed the total volume of α SMA-positive (α SMA+) cells to be significantly lower with actuation compared to the control (** $p=0.0036$, Fig. 5g). This suggests that actuation perturbed the number and likely the function of myofibroblasts in the fibrous capsule.

Neo-vascularization was also assessed in the fibrous capsule by staining for CD31 (Fig. 5h) and counting the number of vessels present around the control and actuated devices. Number per area (Na) and radial diffusion distance (Rd) were all calculated using an unbiased counting frame (41-43). An unpaired students t-test showed a significant increase in the number of CD31+ blood vessels (** $p=0.0099$, Fig. 5i) and a significant decrease in radial diffusion distance for the actuated DSR compared to the non-actuated controls (** $p=0.0009$, Fig. 5j). This indicated an increased vascularity of the capsule following actuation.

In vivo enhancement of therapy delivery with a porous DSR

To investigate the transport of therapy through the resulting fibrous capsule, a therapy analog Genhance (Perkin Elmer) was injected through the therapy delivery catheter of a control and actuated porous DSR and subsequently through the porous membrane to the surrounding tissue at day 8 and 14 (Fig 6a for timeline). Fluorescent *in vivo* imaging was conducted for 1 hour after delivery of drug analog (Fig. 6b). Fluorescence (radiant efficiency) was plotted for each animal for 1 hour post-delivery, for the control and actuated DSR, and the area under the radiant efficiency curve was calculated (Fig. 6c). There was a decrease in the amount of drug analog delivered to an area of tissue surrounding the implant over time, as expected due to the attenuation of drug diffusion due to the FBR (Fig. 6c). However, this reduction was not observed with actuation, as diffusion was not impeded to the same extent. The actuated devices delivered more drug analog compared to the control at each time-point (37% and 16% mean improvement at day 8 and 14 respectively, Fig. 6c). The area of diffusion was also quantified, with the actuated groups showing a larger spatial area of diffusion (in a 2D plane) than the control after one hour at day 8 and day 14 (Fig. 6d).

Demonstration of functional effect due to enhanced delivery through an actuated DSR

As a model therapy to visualize rapid drug delivery, epinephrine was delivered through the control and actuated devices ($n=2$). Using a pressure-volume catheter, we measured the maximum rate of change of the interventricular pressure (dP/dt max is a measure of the contractility of the ventricle) immediately after delivery of the drug. The time to therapeutic effect is defined as the time when the dP/dt max levels off, and stops increasing. This time is indicated by dashed lines for a control and actuated device in the same animal (Fig. 6e), and is lower (~ 40 s) for the actuated device compared to the control (~ 170 s). The cyclical average dp/dt max in the first 40 seconds after delivery is significantly higher ($p<0.001$) in the actuation group compared to the control (Fig. 6f), acting as a clinically responsive model to demonstrate enhanced delivery following the actuation regime. Finally, an osmolarity study (Supplementary Fig. S9) demonstrates that there are no significant dimensional changes to the TPU material or overall device when submerged for up to 1 week in hypotonic and hypertonic solution *in vitro*.

Discussion

In this study we describe milliscale dynamic soft reservoirs that use a mechanocutical approach to actively modulate the biomechanics of the biotic-abiotic interface by perturbing strain and fluid flow. We show, using computational and experimental techniques that the DSR creates

strains up of 6.4% and 8.6% on the non-porous and porous membranes and thereby induces peri-implant fluid flow in close proximity to the device. A parametric study shows the tunability of the platform, and that pressure loading and radius size are both positively correlated to the deflection while material stiffness and membrane thickness are negatively correlated to the deflection. In a 14 day rat study with a non-porous DSR we show a significant reduction in fibrotic capsule thickness with no statistical difference in capsule quality (collagen maturity and coherency). We show a reduction in α SMA myofibroblasts, an increase in the number of CD31+ neo-vessels and a decrease in radial diffusion distance between CD31+ vessels in the actuation group compared to non-actuated controls. We demonstrate that this reduction in FBR can cause enhanced pharmacokinetics in a porous DSR incorporating a drug delivery component where we show an improvement in the amount and the area of diffusion at day 8 and day 14. To demonstrate a functional effect with a model pharmacological agent, we deliver an inotropic drug, epinephrine, through a porous DSR, and show that we can increase cardiac contractility and developed pressure more efficiently and quickly in the actuated group compared to the control, likely due to the reduced fibrous capsule in the actuated DSR.

This implantable device uses the principals of soft robotics to cyclically actuate a flexible membrane that modulates the biomechanics of the biotic-abiotic interface. This approach takes advantage of controlled mechanical actuation to elicit a specific biological response and as such reduces fibrotic encapsulation of implantable medical devices. An unwanted 50-200 μ m thick fibrotic capsule has been reported to build up (<1 month) and envelope implanted devices (25, 44), which can be detrimental to the function of the device and cause significant pain and discomfort to the patient (44, 45). The fibrous capsule thickness reported in this study for the non-actuated control falls within this range (control = 0.1047 ± 0.0314 mm,) whereas we show a significant \sim 2-fold reduction in thickness with actuation (actuated = 0.05218 ± 0.0151 mm, *** $p=0.0005$). We show that there is no statistical difference in the collagen content of the resulting fibrous capsule ($p>0.05$) meaning that we report a thinner capsule with no difference in quality.

Macrophages have been shown to be a key driver of the fibrotic response (25) and strain has been shown to modulate macrophage polarization to pro-inflammatory or pro-healing phenotypes (33). In this study, computational models predict maximum strain levels of 6% on the functional membrane of the reservoir, which is below the strain shown to cause macrophage detachment (12%) (33). In agreement with this, we found no biologically relevant difference in the numerical density of macrophages at the interface when quantified by CD68 staining in the actuation group compared to the control (45417 ± 16799 vs 67024 ± 23976 , $p=0.6983$). The maximum strain predicted in this study (6.4% for non-porous membranes, 8.4% for porous membranes) is similar to results by Ballotta et al. who show activation towards the pro-healing (M2) phenotype at 7% strain (33), which could potentially explain the reduced fibrous capsule thickness we report. Interestingly, strain and fluid flow are also known to have distinct effects on fibroblasts and myofibroblasts during healing processes (46). Cyclic mechanical loading has been shown to reduce myofibroblast differentiation of primary lung fibroblasts (47) and growth and repair processes of the heart are guided by mechanical stimuli (48, 49). These results suggest that actuation could be a potential mechanistic target to modulate extra cellular matrix (ECM) synthesis in fibrotic capsule formation and contracture. Here we show a significant reduction in the number of α -SMA+ myofibroblasts ($p=0.0036$) with no change in CD68+ macrophages ($p=0.6963$) in the actuated group compared to the control, and we propose that actuation mediated strain of the cells present in the capsule reduces differentiation and proliferation of myofibroblasts and therefore ECM production and overall capsule thickness. Our *in vitro* investigation of the WPMY-1 myofibroblast cell line shows that actuation does not significantly affect metabolic activity or cell viability and results in a downward trend in collagen production/cell. However, it is difficult to recapitulate innate host responses at a single *in vitro* cellular component level as it does not capture the complex signaling environment between macrophages, myofibroblasts and many other cells during the fibrotic cascade, for this reason we focused on the *in vivo* outcomes in this study. Although the bulk in-plane strains shown in this study may not be experienced at the cellular level

initially, mechanical forces and strains will be transduced as a connected fibrous capsule matures around the implant.

In a previous study we report a replenishable implanted epicardial reservoir and have shown that despite the formation of a fibrous capsule (which hinders but does not impede diffusion), molecules with a range of molecular weights can be transported through the membrane into the tissue (39). In this study we show an improvement point (37% and 16% mean improvement at day 8 and 14 respectively) in diffusion of a therapy analog through the fibrous capsule compared to the control. This improvement in diffusion is particularly important in the field of cell and drug delivery to treat Type 1 Diabetes, specifically for cell encapsulation strategies where rapid diffusion of glucose and insulin is required (50, 51). Modified alginate spheres encapsulating stem-cell derived beta-cell have been shown to reduce fibrosis and result in long term glycemic control in mice (22, 23, 25). The replenishable nature of the therapeutic DSR, with a reduced FBR following actuation, offers a number of advantages over biomaterial encapsulation as it allows for i) top-up and refill ii) multiple dose forms and iii) multi-cargo delivery that can be tailored to patient need.

There are some limitations with the current study. Here, we list these shortcomings, and suggest further steps that need to be taken to realize clinical translation of the DSR. First, our sample sizes for this proof-of-concept study were small, and therefore the study is more of a demonstration that a dynamic reservoir can affect host response than a preclinical study designed for a specific clinical application. Longer-term *in vivo* studies with increased sample sizes will be required to study the long-term effects of this kind of therapy including how responses change once actuation ceases. For moving towards clinical translation, we aim to use a refined implantable pump (Fig. 1a, Supplementary Fig. S1, Supplementary Movie S1). Ultimately, we plan to power and control this pump using wireless technology. Second, more complex, closed-loop interaction with the host could be added, for example triggering actuation when the implant senses specific cellular activity on the functional membrane. Leveraging the ongoing miniaturization of sensors (52, 53), and the continuing evolution of techniques for wireless communication and power transfer (54, 55), and energy scavenging (56) will allow us to modify the device to achieve this control.

In conclusion, this work demonstrates the ability for dynamic implantable devices to affect the host response to medical implants. We show two configurations of this strategy to demonstrate the potential of this device. The impermeable, non-porous configuration could be incorporated in a sheath as a surface modification for implants with a structural role such as breast implants and pacemaker leads, preventing capsular contraction. The permeable, porous configuration improves the transport of therapy into the tissue, which is desirable for drug/cell delivery or biosensing applications. As such, we suggest that these soft, mechanoceutical devices could lead to a myriad of implantable, application-specific soft robots, specifically designed to study, or treat clinical conditions. If we can harness this phenomenon to address clinically adverse issues that are commonplace with implanted devices, the strategy can lead to vast opportunities for the field of soft robotics in fine-tuning the biological host response.

Materials and Methods

Study Design

The overall objective of the study was to demonstrate that actuation of an implantable reservoir (DSR) modulates the foreign body response. Our control group was a static implanted DSR and our treatment group was an actuated DSR (actuated to 1-2 psi for 5 minutes every 12 hours for 14 days). We conducted an *in vitro* study with control and treatment DSRs seeded with a myofibroblast cell line and analyzed cell viability, metabolic response and collagen deposition with LDH cytotoxicity assay, Alamar Blue metabolic activity assay and Sircol™ soluble collagen assay respectively. A time-point of 14 days was used based on previous studies assessing fibrotic encapsulation of materials (25, 27). We then conducted two *in vivo* studies. The first was with a non-porous version of the DSR, with the objective of measuring fibrous capsule thickness, quality and composition. We implanted two devices per animal, with a sample size of 3-6. Control and treatment groups were paired as far as possible to enhance statistical power, given the low sample

size. To measure thickness, we conducted microCT analysis, with subsequent thresholding and segmentation in Mimics software (Materialise). Up to 4000 measurements were made of the thickness of the fibrous capsule, and analysis was repeated by two blinded operators. We then conducted immunohistochemistry for macrophage content, blood vessel content. Again two blinded counters were used for each analysis. For the second *in vivo* study we used a porous version of the DSR, with the objective of measuring the amount of drug delivered through an actuated and control DSR at day 8 and day 14 post-implantation, to assess whether the decreased fibrous capsule affected cargo delivery through the device. We used a therapy analog Genhance and measured the amount of analog delivered, and the spread of the drug in each group by quantifying fluorescence at day 8 and 14. Again, a sample size of 3-6 was used. The control and treatment groups were paired within animals where possible, to allow paired statistical analysis. We then did a proof-of-concept study with one animal to show that a pharmacological agent (epinephrine) could diffuse through the capsule, and this exert its action more rapidly in the treatment group.

DSR fabrication

The device manufacture technique for the individual reservoirs is shown in Supplementary Fig. S3. Briefly, 0.075 mm and 0.3 mm thick TPU sheets (HTM-8001-M and HTM-1001 polyether TPU film, American Polyfilm, Inc) were formed into hemispherical shapes, with a height of 3.9 mm and a diameter of 3.5 mm, using a vacuum thermal former (Yescom Dental Vacuum Former, Generic). 0.075 mm thick TPU hemispheres were placed inside the 0.3 mm thick TPU hemispheres and 7 cm of 3 Fr thermoplastic polyurethane catheter tubing (Micro-Renathane MRE037 0.037" x 0.023, Braintree scientific) was bonded to this assembly using a heat transfer machine (Heat Transfer Machine QXAI, Powerpress). This forms the actuation reservoir, which was used for actuating the system with pneumatic pressure via the catheter. A 0.075 mm thick TPU membrane and a second 9 cm 3 Fr thermoplastic polyurethane catheter was then bonded onto this assembly to form the therapy reservoir which can be used to deliver therapeutics prior to or post implantation via the catheter. This reservoir interfaces with soft tissue via the TPU membrane which can either be nonporous or porous (Fig. 1b). 10 μm pores (National Centre for Laser Applications, National University of Ireland Galway) were used in this study to minimize fluid flow into the DSR therapy reservoir during actuations. The size and shape of the DSR can be easily altered by modifying the positive and negative 3D printed molds as shown in Supplementary Fig. S3.

Implantable system

A fully implantable peristaltic pump (Dolomite 3200243) was used for cyclic actuation of DSRs. The device was placed in series with the outflow tube of the pump. A TinyLily mini processor (TinyCircuits ASM2101) and TinyLily motor board (TinyCircuits ASL2001) connected via a custom printed circuit board (Oshpark) were used to regulate pumping. The entire assembly was powered by a small 3.7 V, lithium ion battery (Adafruit 2011). Running a customized program written in Arduino, the control system can turn the pump on for an adjustable period of time then reverse the direction of electric current, causing it to pump in reverse for another adjustable time interval. Calibration of the forward /reverse cycles enabled cyclic actuation at a variety of desired pressures and peak forces. We tuned the force and frequencies to match that of the external control box, and measured the cyclical force with an Instron (Supplementary Fig. S1).

Experimental characterization of the DSR

Uniaxial tensile tests (according to ASTM D638) were performed on a Zwick Roell material testing machine with laser cut TPU specimens. Using the material evaluation feature in Abaqus 2018 (Dassault Systèmes, Vélizy-Villacoublay, France), four hyperelastic constitutive models (Neo-Hookean, Yeoh, Mooney-Rivlin and Ogden 3rd order) were evaluated. As shown in Fig. 3b, the Ogden 3rd order model had excellent curve fitting performance and therefore was used for the model. The strain energy density function is shown in Supplementary Fig. S5c. The actuation force of the device was measured using an Instron 5944 material testing machine. The set-up is shown in

Supplementary Fig. S5. An acrylic test-rig (Supplementary Fig. S5) was laser cut to allow the lower membrane of the device to contact the upper compression plate for force measurement. The thickness of the acrylic piece (10 mm) and the diameter of the hollow cylinder (5 mm) were designed to be larger than the height and the diameter of the outer membrane allowing unconstrained deformation of the reservoir. The distance between the compression plates was fixed at the thickness of the acrylic holder. The force was measured using a 50 N load cell. To test the effect of fatigue on the devices 100,000 cycles at 1 psi and 2 psi at 1 Hz was applied to non-porous DSR *in vitro* and burst pressure testing was carried out (n=6/group). A pressure sensor (Truwave intravascular disposable pressure sensors, Edwards) with an amplifier (instrument amplifier INA125P, Digikay) and an Arduino UNO interface was connected to the device and syringe via a T-valve. A syringe pump (PHD Ultra, Harvard Apparatus) was used to inflate the devices to failure and burst pressure was recorded.

Computational modelling

All simulations were conducted in the commercially available software, Abaqus 2018 (Dassault Systèmes, Vélizy-Villacoublay, France). Since the reservoir is comprised of thin thermoplastic polyurethane sheets, shell structural analysis was chosen for the simulation. The device was modeled as a 3D surface geometry, which contains the outer, middle and lower membrane, as shown in Supplementary Fig. S5. The appropriate thickness of each shell was assigned. All parts were meshed with 2603 four-node shell elements (S4R). Dirichlet boundary conditions were applied to the protruding edge of the lower membrane and all other surfaces were allowed to deform freely. A 2 psi ramp loading was applied to the internal surface of the inner and outer membranes for a duration of 500 ms. These boundary conditions were representative of the *in vivo* scenario when the reservoir was sutured to the muscular tissue by the edge of the lower membrane and actuated with a cyclic pressure with magnitude of 2 psi and 1 Hz.

We also created a fluid structure interaction model using the smooth particle hydrodynamics (SPH) technique to study the effect of actuation on surrounding fluid flow (Fig. 3h and i). A $20 \times 20 \times 5 \text{ mm}^3$ region was created and filled with 8000 particles. The particles were assigned with a density of $9.96 \times 10^{-7} \text{ kg/mm}^3$, bulk modulus of 20.94 MPa and dynamic viscosity of $3.56 \times 10^{-8} \text{ MPa.s}$. Contact pairs were initiated between the shell structure and the particles. Loading and boundary conditions of the shell were the same as the structural analysis.

In vitro studies

WPMY-1 myofibroblast cell line (ATCC CRL-2845) was cultured in high glucose DMEM-D5671 (Sigma, Ireland) supplemented with 5% Fetal Bovine Serum, 1% Penicillin/Streptomycin and 0.05% L-glutamine. The non-porous membranes of the DSR was soaked in 150 μL FBS for 2 hours. The FBS was then washed off with PBS and myofibroblasts were seeded on the non-porous membranes of the DSRs at 25,000 cells/device and cultured for 24 hours (37°C, 5% CO₂). The DSR was actuated to 1-2 psi at 1 Hz for 5 mins every 12 hrs for 14 days and metabolic activity, cell viability and soluble collagen production was compared to non-actuated controls at day 3, 7, 10 and 14. Metabolic activity was assessed using Alamar Blue assay as previously described (57), cell viability was assessed using LDH cytotoxicity assay, and collagen production was assessed using Sircol™ soluble collagen assay following the manufacturers protocols. Devices were fixed with 4% PFA for 10 min and then washed 3 times in 1X PBS before permeabilization of the cells with 0.15% Triton in 1X PBS for 2 min. Devices were washed 3 times in 1X PBS and blocked in 1% bovine serum albumin (BSA) for 30 min before staining with Alexa Fluor™ 488 Phalloidin (Thermo Sci Cat no: A12379) at 1:200 dilution for 60 min. Devices were washed 3 times in 1X PBS before counter staining with Hoechst at 1:1000 dilution for 10 min. Devices were then mounted using fluoromount (Sigma, F4680) and observed using a spinning disc inverted confocal microscope (Yokagawa CSU22) combined with Andor iQ 2.3 software.

In vivo studies

Animal procedures were reviewed and approved according to ethical regulations by the Institutional Animal Care and Use Committees at Massachusetts Institute of Technology. Female Sprague Dawley rats (225–300 g) were anaesthetized using isoflurane (1–3% isoflurane in oxygen). Animals were treated with a single dose of sustained release buprenorphine (Bup-SR) at 1 mg/kg subcutaneously to control pain. 2 DSR devices (porous or non-porous) were implanted subcutaneously in the rat, the device implantation procedure is shown in Supplementary Fig. S8. Briefly, the hair on the back of the rat was removed and surgical sites were prepared with 3 washes of Betadine and 70% ethanol. Devices were sterilized using ethylene oxide prior to implantation. An anterior incision was made at the base of the neck for the and 2 posterior incisions were made 9 cm from the original incision along the back of the rat, 1 cm lateral of the spine. A blunt dissection was made at all incisions and a forceps was used to tunnel subcutaneously from the anterior to the posterior sites. A vascular access button, or self-sealing subcutaneous port (VAB95BS-MRI, VABM2B/22R22, VABR4B/22 Instech Laboratories), was connected to the dorsal end of the catheter of each DSR. The port was placed in position at the base of the neck and the devices tunneled posteriorly into position. The port was secured to the underlying fascia using at least one interrupted suture (5-0 monofilament). Each DSR was secured to the underlying fascia with one suture at either side (7-0 monofilament). The skin was closed with interrupted sutures (5-0 monofilament) and the animal was allowed to recover on a heated pad. 3 mL of warm saline were administered subcutaneously. The following day, one of the two implanted DSR devices was actuated at controlled input pressures of 1 psi (regime 1) or 2 psi (regime 2) at 1 Hz every 12 hours for 14 days (Fig. 5a, Fig. 7a) and compared to the non-actuated control reservoir for analysis. On day 14 animals were sacrificed by CO₂. Following sacrifice, each device and the immediate surrounding tissue were extracted. Tissues were fixed for 24 h using 10% Formalin (pH 7.4). The tissue was then washed in 0.2 M phosphate-buffered saline with a final wash in 70% ethanol.

IVIS imaging

On days 8 and 14, diffusion of a fluorescent imaging agent (Genhance 750 Fluorescent Imaging Agent, NEV10118, Perkin Elmer) out of the porous DSR devices was evaluated using an IVIS Spectrum-bioluminescent and fluorescent imaging system (Perkin Elmer). Images were acquired using a 745 nm/800 nm excitation-emission filter pair. Prior to injection of agent, the line was cleared by establishing vacuum with a syringe connected to the subcutaneous port. The skin above the DSR area was shaved and marked to aid with region of interest (ROI) placement for quantitative analysis. After a background image was acquired, 35 μ L of fluorescent agent were injected through the subcutaneous port either manually or with a syringe-pump (150 μ L/min, Harvard Apparatus). Images were acquired for up to 1 hour following injection ~ every 3 min. An ROI (28.24 pixel diameter circle) was placed at the center of each DSR in each image and the total radiant efficiency was measured using the Living Image 3.2 software. The total radiant efficiency measured immediately after injection was subtracted from the subsequent measurements to account for the change in radiant efficiency due to diffusion over time. For the measurement of diffusion area, the color range of IVIS images obtained immediately after injection and after 1 h of diffusion was adjusted such that delineation of the areas of interest was possible. The adjusted image files were imported into ImageJ and the corresponding diffusion areas were delineated using the polygon tool and quantified. The area measured immediately after injection was subtracted from the area measured after diffusion.

Functional measurements following epinephrine injection

To illustrate how actuation can improve the time to functional effect after small-molecule delivery, 35 μ L of epinephrine (1 mg/mL) was delivered through the porous DSR while recording blood pressure with an apically inserted pressure–volume catheter (Millar) and PowerLab (AD Instruments) as previously described (39). Using the pressure/volume data, and the PV module in LabChart software (AD Instruments) we plotted dP/dt max, an index of contractility over time for

10 minutes after injection for a control or actuated device. We then calculated the developed pressure per cycle for each device.

microCT, histological and immunohistochemical analysis

For microCT analysis, fixed tissue samples were transferred to a 2.5% PMA solution in 70% ethanol for 7 days, then washed and stored in fresh 70% ethanol. MicroCT images were captured using a μ CT 100 scanner (Scanco) at 70 kVp and 85 μ A with a 0.5mm Aluminum filter. microCT dicom files were segmented using Mimics Research 18.0.0.525 software as described in Supplementary Material.

Fixed tissue samples (n=3-6 animals/group) were transected in half, orientated and embedded in paraffin wax blocks for histological and immunohistochemical analysis. Sections of 5 μ m were cut, deparaffinised in xylene, and rehydrated through a series of graded alcohols. For histological fibrotic capsule quality analysis, sections were stained with 0.1% Picrosirius red/fast green solution (1:1) using an automated stainer (Leica ST5010 Autostainer XL). Slides were imaged using Ocular².0 Imaging Software on an Olympus BX41 Microscope with Olympus U-AN360P analyzer under a 20x objective lens. Quantification of the collagen content was performed using a previously reported technique (58, 59). For immunohistochemical analysis, primary antibodies of CD31 (ab28364, Abcam) (1:200), CD68 (MCA341, Bio Rad) (1:300) and α -SMA (ab5694, Abcam) (1:100) were incubated for 1 hour at 37 °C. Secondary antibodies of Alexa Fluor[®] 594 goat anti-mouse IgG (ThermoFisher Scientific) (1:200), Alexa Fluor[®] 594 goat anti-rabbit IgG (ThermoFisher Scientific) (1:200) and Alexa Fluor[®] 488 goat anti-mouse IgG (ThermoFisher Scientific) (1:200) were incubated for 60 min at room temperature, respectively. Sections were stained with Hoechst and coverslipped using fluoromount. Immunofluorescence-stained slides were observed using a spinning disc inverted confocal microscope (Yokagawa CSU22) combined with Andor iQ 2.3 software. Analysis of Macrophages: 20 random fields of view were acquired from 8 sections using confocal microscopy. Using stereological methods an unbiased estimation of area fraction and numerical density (N_v) was calculated (40-42). Numerical density refers to the number of, in this case macrophages, within a unit volume of tissue. Analysis of Myofibroblasts: 20 random fields of view were acquired from 8 sections using confocal microscopy. Area Fraction was estimated using Image J (Fiji version 2.0.0) software. This was done by way of auto thresholding using the otsu filter which eliminates autofluorescence and calculates the area fraction of tissue occupied by α SMA+ cells. The area fraction was then multiplied by the average volume of the region of interest in both control and regime groups to provide an estimate of the total volume of α SMA+ cells to assess whether the presence of myofibroblasts were perturbed by actuation. Analysis of neo-vascularization: Number per area (N_a) and radial diffusion distance (R_d) were calculated using an unbiased counting frame (41-43). This counting frame consists of red forbidden lines and green acceptance lines. Any blood vessel that is cut by a forbidden line is not counted. Blood vessels that appear outside the counting frame or are cut by the acceptance lines without also cutting the forbidden line are counted. The application of this counting formula generates an unbiased estimate of the number of blood vessels per unit area. $N_a = cN / (cPts \times \text{Area of Grid})$ taking cN as the cumulative no. of blood vessels counted and cPts as the cumulative no. of points. The length density (L_v) of a blood vessel is the length of blood vessels present per unit volume and is calculated by multiplying the numerical density by 2. From length density the radial diffusion distance (R_d) can be calculated by the following formulas: $L_v = N_a \times 2$, $R_d = 1 / \sqrt{(\pi(L_v))}$.

Statistical Analysis

GraphPad Prism (8.1.0) or Stata version 16.0 was used for statistical analysis. Non-parametric tests are sometimes performed for n \leq 3 per group, in part because the sample is too small to test whether the endpoint is normally distributed. However, the t-test is fairly robust to departures from normality, and in many circumstances it is more powerful than corresponding non-parametric tests (60). Thus, we conducted t-tests (or generalizations of t-tests, as we explain) to compare endpoint measurements between the control and actuated samples. Where possible, when each

animal had both a control and actuated device, we used paired t-tests. For endpoints for which some animals had data only under control or only under actuated conditions, we fit linear regression models in a generalized estimating equations (GEE) framework, with robust standard errors and an independent correlation structure (61). The GEE model can be thought of as being similar to the paired t-test while allowing an unbalanced design and accounting for the correlated data caused by having control and actuated measurements in the same animals. To maximize study sensitivity, we considered the primary analysis to have only two comparison groups, i.e. we collapsed data from regime 1 and 2 into one treated group (actuation). We consider the comparison of measurements between two regimes (e.g. two different pressure levels) as exploratory, i.e. we do not consider the p-value a dichotomous significance test. For burst pressure and osmolarity analyses, there were more than two groups. First, normality was tested with a Shapiro-Wilk test, if the data were normally distributed a one-way or two-way analysis of variance (ANOVA) with Tukey's *posthoc* adjustment for multiple comparisons. If the data were not normally distributed a Kruskal Wallis test was used with Dunn's *posthoc* adjustment for multiple comparisons. Statistical significance was accepted when $p < 0.05$.

List of Supplementary Materials

Supplementary Materials and Methods

Supplementary Figure S1: Implantable actuation system

Supplementary Figure S2: Non porous DSR arrays to reduce complications associated with implantable devices.

Supplementary Figure S3: Device manufacture procedure which involves two step –thermoforming and heat sealing.

Supplementary Figure S4: Test set-up for force characterization and porous vs non-porous computational models.

Supplementary Figure S5: Analytical approximation for large deflection circular plate.

Supplementary Figure S6: Parametric study using large deflection plate analytical approximation.

Supplementary Figure S7: *In vitro* assessment of the effect of actuation of non-porous DSR on myofibroblasts cell line (WPMY-1).

Supplementary Figure S8: Pre-clinical implementation of the DSRs.

Supplementary Figure S9: The dimensional effects of submerging the device, and its constituent material in saline with different concentrations.

Supplementary Movie S1: Actuation of DSR with implantable pump.

Supplementary Movie S2: Actuation of low profile non-porous DSR.

Supplementary Movie S3: Actuation of DSR *in vivo*.

References and Notes

1. F. Lotti, F. Ranieri, G. Vadalà, L. Zollo, G. Di Pino, Invasive Intraneural Interfaces: Foreign Body Reaction Issues. *Frontiers in neuroscience* **11**, 497-497 (2017).
2. T. D. Y. Kozai, A. S. Jaquins-Gerstl, A. L. Vazquez, A. C. Michael, X. T. Cui, Brain tissue responses to neural implants impact signal sensitivity and intervention strategies. *ACS chemical neuroscience* **6**, 48-67 (2014).
3. N. Cetin, N. M. Sav, E. Ciftci, B. Yildiz, Foreign Body Reaction to Dialysis Catheter and Peritoneal Fluid Eosinophilia in a Child on Continuous Ambulatory Peritoneal Dialysis. *Iranian journal of kidney diseases* **11**, 319-321 (2017).
4. X. Liu *et al.*, Comparison of the postoperative incidence rate of capsular contracture among different breast implants: a cumulative meta-analysis. *PloS one* **10**, e0116071 (2015).
5. K. G. Tarakji, C. R. Ellis, P. Defaye, C. Kennergren, Cardiac implantable electronic device infection in patients at risk. *Arrhythmia & electrophysiology review* **5**, 65 (2016).
6. A. A. Sharkawy, B. Klitzman, G. A. Truskey, W. M. Reichert, Engineering the tissue which encapsulates subcutaneous implants. I. Diffusion properties. *Journal of Biomedical Materials Research Part A* **37**, 401-412 (1997).
7. M. T. Novak, F. Yuan, W. M. Reichert, Modeling the relative impact of capsular tissue effects on implanted glucose sensor time lag and signal attenuation. *Analytical and bioanalytical chemistry* **398**, 1695-1705 (2010).
8. V. Thome-Duret, M. Gangnerau, Y. Zhang, G. Wilson, G. Reach, Modification of the sensitivity of glucose sensor implanted into subcutaneous tissue. *Diabetes & Metabolism* **22**, 174-178 (1996).
9. W. M. Fritschy, A. Pasma, G. Wolters, R. Schilfgaard, H. G. Klatter, The capsular overgrowth on microencapsulated pancreatic islet graft in streptozotocin and autoimmune diabetic rats. *Transplant international* **7**, 264-271 (1994).
10. P. Soon-Shiong *et al.*, in *Transplantation proceedings*. (1991), vol. 23, pp. 758-759.
11. A. A. Sharkawy, B. Klitzman, G. A. Truskey, W. M. Reichert, Engineering the tissue which encapsulates subcutaneous implants. III. Effective tissue response times. *Journal of Biomedical Materials Research Part A* **40**, 598-605 (1998).
12. A. A. Sharkawy, B. Klitzman, G. A. Truskey, W. M. Reichert, Engineering the tissue which encapsulates subcutaneous implants. II. Plasma-tissue exchange properties. *Journal of Biomedical Materials Research Part A* **40**, 586-597 (1998).
13. A. M. Research. (Global Opportunity Analysis and Industry Forecast 2014-2022, 2018).
14. W. K. Ward. (SAGE Publications, 2008).
15. D. T. Luttkhuizen, M. C. Harmsen, M. J. V. Luyn, Cellular and molecular dynamics in the foreign body reaction. *Tissue engineering* **12**, 1955-1970 (2006).
16. J. Anderson, K. Defife, A. McNally, Monocyte, macrophage and foreign body giant cell interactions with molecularly engineered surfaces. *Journal of Materials Science: Materials in Medicine* **10**, 579-588 (1999).
17. J. M. Anderson, A. Rodriguez, D. T. Chang, Foreign body reaction to biomaterials. *Seminars in Immunology* **20**, 86-100 (2008).
18. Y. M. Ju, B. Yu, L. West, Y. Moussy, F. Moussy, A dexamethasone-loaded PLGA microspheres/collagen scaffold composite for implantable glucose sensors. *Journal of Biomedical Materials Research Part A* **93**, 200-210 (2010).
19. A. Koh, S. P. Nichols, M. H. Schoenfisch, Glucose sensor membranes for mitigating the foreign body response. *Journal of Diabetes Science and Technology* **5**, (2011).
20. R. J. Soto, B. J. Privett, M. H. Schoenfisch, In vivo analytical performance of nitric oxide-releasing glucose biosensors. *Analytical chemistry* **86**, 7141-7149 (2014).
21. R. J. Soto, E. P. Merricks, D. A. Bellinger, T. C. Nichols, M. H. Schoenfisch, Influence of diabetes on the foreign body response to nitric oxide-releasing implants. *Biomaterials* **157**, 76-85 (2018).

22. A. J. Vegas *et al.*, Long-term glycemic control using polymer-encapsulated human stem cell-derived beta cells in immune-competent mice. *Nature medicine* **22**, 306-311 (2016).
23. M. A. Bochenek *et al.*, Alginate encapsulation as long-term immune protection of allogeneic pancreatic islet cells transplanted into the omental bursa of macaques. *Nature Biomedical Engineering*, 1 (2018).
24. R. Robitaille *et al.*, Studies on small (< 350 μm) alginate-poly-L-lysine microcapsules. III. Biocompatibility of smaller versus standard microcapsules. *Journal of Biomedical Materials Research* **44**, 116-120 (1999).
25. O. Veisoh *et al.*, Size-and shape-dependent foreign body immune response to materials implanted in rodents and non-human primates. *Nature materials* **14**, 643 (2015).
26. B. F. Matlaga, L. P. Yasenchak, T. N. Salthouse, Tissue response to implanted polymers: the significance of sample shape. *Journal of Biomedical Materials Research Part A* **10**, 391-397 (1976).
27. J. C. Doloff *et al.*, Colony stimulating factor-1 receptor is a central component of the foreign body response to biomaterial implants in rodents and non-human primates. *Nature Materials*, (2017).
28. Y. Ito *et al.*, Nano-vibration effect on cell adhesion and its shape. *Bio-medical materials and engineering* **21**, 149-158 (2011).
29. G. A. Truskey, J. S. Pirone, The effect of fluid shear stress upon cell adhesion to fibronectin-treated surfaces. *Journal of biomedical materials research* **24**, 1333-1353 (1990).
30. I. R. Titze, S. A. Klemuk, X. Lu, Adhesion of a monolayer of fibroblast cells to fibronectin under sonic vibrations in a bioreactor. *Annals of Otolaryngology & Laryngology* **121**, 364-374 (2012).
31. M. E. Stamp *et al.*, Exploring the Limits of Cell Adhesion under Shear Stress within Physiological Conditions and beyond on a Chip. *Diagnostics* **6**, 38 (2016).
32. W. J. Kao, Evaluation of leukocyte adhesion on polyurethanes: the effects of shear stress and blood proteins. *Biomaterials* **21**, 2295-2303 (2000).
33. V. Ballotta, A. Driessen-Mol, C. V. Bouten, F. P. Baaijens, Strain-dependent modulation of macrophage polarization within scaffolds. *Biomaterials* **35**, 4919-4928 (2014).
34. C. A. Cezar *et al.*, Biologic-free mechanically induced muscle regeneration. *Proceedings of the National Academy of Sciences* **113**, 1534-1539 (2016).
35. P. Polygerinos *et al.*, Soft robotics: Review of fluid-driven intrinsically soft devices; manufacturing, sensing, control, and applications in human-robot interaction. *Advanced Engineering Materials* **19**, 1700016 (2017).
36. E. T. Roche *et al.*, Soft robotic sleeve supports heart function. *Science translational medicine* **9**, eaaf3925 (2017).
37. M. A. Horvath *et al.*, Towards Alternative Approaches for Coupling of a Soft Robotic Sleeve to the Heart. *Annals of biomedical engineering*, (2018).
38. M. A. Horvath *et al.*, An Intracardiac Soft Robotic Device for Augmentation of Blood Ejection from the Failing Right Ventricle. *Annals of biomedical engineering* **45**, 2222-2233 (2017).
39. W. Whyte *et al.*, Sustained release of targeted cardiac therapy with a replenishable implanted epicardial reservoir. *Nature Biomedical Engineering*, (2018).
40. C. Howard, M. Reed. (QTP Publications, 2010).
41. E. Jensen, H. Gundersen, The stereological estimation of moments of particle volume. *Journal of applied probability* **22**, 82-98 (1985).
42. P. Dockery, J. Fraher, The quantification of vascular beds: a stereological approach. *Experimental and molecular pathology* **82**, 110-120 (2007).
43. N. N. Madigan *et al.*, Comparison of cellular architecture, axonal growth, and blood vessel formation through cell-loaded polymer scaffolds in the transected rat spinal cord. *Tissue Engineering Part A* **20**, 2985-2997 (2014).

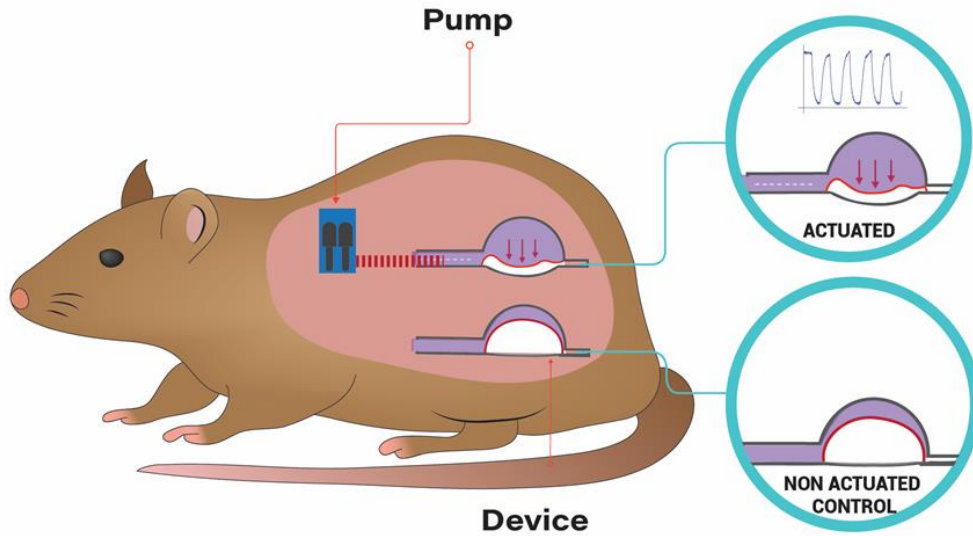
44. B. D. Ratner, Reducing capsular thickness and enhancing angiogenesis around implant drug release systems. *Journal of Controlled Release* **78**, 211-218 (2002).
45. J. D. Bryers, C. M. Giachelli, B. D. Ratner, Engineering biomaterials to integrate and heal: the biocompatibility paradigm shifts. *Biotechnology and bioengineering* **109**, 1898-1911 (2012).
46. S. van Putten, Y. Shafieyan, B. Hinz, Mechanical control of cardiac myofibroblasts. *Journal of molecular and cellular cardiology* **93**, 133-142 (2016).
47. M. E. Blaauboer, T. H. Smit, R. Hanemaaijer, R. Stoop, V. Everts, Cyclic mechanical stretch reduces myofibroblast differentiation of primary lung fibroblasts. *Biochemical and biophysical research communications* **404**, 23-27 (2011).
48. L. A. Taber, Biomechanics of cardiovascular development. *Annual review of biomedical engineering* **3**, 1-25 (2001).
49. P. Patwari, R. T. Lee, Mechanical control of tissue morphogenesis. *Circulation research* **103**, 234-243 (2008).
50. E. Dolgin, Diabetes: Encapsulating the problem. *Nature* **540**, S60-S62 (2016).
51. E. Dolgin. (Nature Publishing Group, 2014).
52. L. Xu *et al.*, 3D multifunctional integumentary membranes for spatiotemporal cardiac measurements and stimulation across the entire epicardium. *Nature communications* **5**, 3329 (2014).
53. M. Kubon *et al.*, Multimodal Chemosensor-Based, Real-Time Biomaterial/Cell Interface Monitoring. *Advanced Biosystems* **2**, 1700236 (2018).
54. S. H. Lee *et al.*, Implantable batteryless device for on-demand and pulsatile insulin administration. *Nature communications* **8**, 15032 (2017).
55. J. Kim *et al.*, Battery-free, stretchable optoelectronic systems for wireless optical characterization of the skin. *Science advances* **2**, e1600418 (2016).
56. B. Lu *et al.*, Ultra-flexible piezoelectric devices integrated with heart to harvest the biomechanical energy. *Scientific reports* **5**, 16065 (2015).
57. E. B. Dolan *et al.*, Advanced Material Catheter (AMCath), a minimally invasive endocardial catheter for the delivery of fast-gelling covalently cross-linked hyaluronic acid hydrogels. *Journal of biomaterials applications*, (2018).
58. M. G. Monaghan *et al.*, Exogenous miR-29B Delivery Through a Hyaluronan-Based Injectable System Yields Functional Maintenance of the Infarcted Myocardium. *Tissue Eng Part A* **24**, 57-67 (2018).
59. E. B. Dolan *et al.*, A bioresorbable biomaterial carrier and passive stabilization device to improve heart function post-myocardial infarction. *Materials Science and Engineering: C* **103**, 109751 (2019).
60. J. C. De Winter, Using the Student's t-test with extremely small sample sizes. *Practical Assessment, Research & Evaluation* **18**, (2013).
61. K.-Y. Liang, S. L. Zeger, Longitudinal data analysis using generalized linear models. *Biometrika* **73**, 13-22 (1986).
62. Y. Zhang, Large deflection of clamped circular plate and accuracy of its approximate analytical solutions. *Science China Physics, Mechanics & Astronomy* **59**, 624602 (2016).
63. S. Timoshenko, S. Woinowsky-Krieger. (McGraw-Hill Book Company, New York, 1959).

Acknowledgments: The authors would like to acknowledge the support of the Centre of Microscopy and Imaging (NUI Galway) and the Koch Imaging Core (MIT) for imaging expertise. The authors would also like to thank Mark Canney, Kerry Thompson and David Connolly for imaging technical support and Thibault Fresneau, Markus Horvath, Raymond O'Connor, Jack Murphy, Jackson Hardin and James Prendergast for research assistance. **Funding:** ETR acknowledges funding from the Mechanical Engineering Department and the Institute for Medical Engineering and Science at the Massachusetts Institute of Technology. WW, STR and GPD

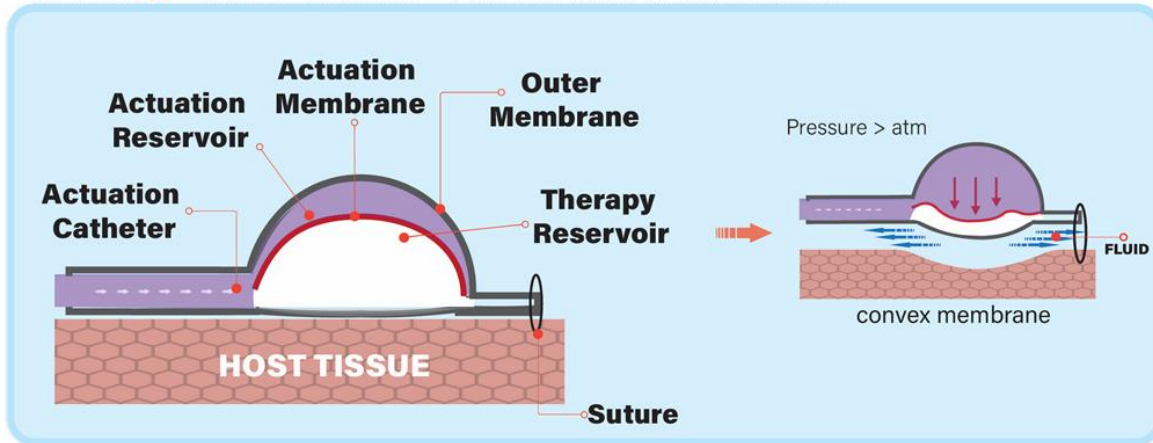
acknowledge funding from Science Foundation Ireland under grant SFI/12/RC/2278, Advanced Materials and Bioengineering Research (AMBER) Centre, National University of Ireland and Trinity College Dublin, Ireland. GPD, RL and EM acknowledge financial support from the National University of Ireland Galway. EBD and GPD acknowledge The DRIVE project which has received funding from the European Union's Horizon 2020 research and innovation program under grant agreement number 645991. EBD and GPD acknowledges funding from European Molecular Biology Organization Short Term Fellowship. STR has received funding from the European Union's Horizon 2020 research and innovation program under the Marie Skłodowska-Curie grant agreement No. 713567. CEV acknowledges the financial support from the National Science Foundation Graduate Research Fellowship Program. Any opinions, findings, and conclusions or recommendations expressed in this material are those of the author(s) and do not necessarily reflect the views of the National Science Foundation. This work was conducted with support from Harvard Catalyst | The Harvard Clinical and Translational Science Center (National Center for Advancing Translational Sciences, National Institutes of Health Award UL 1TR002541) and financial contributions from Harvard University and its affiliated academic healthcare centers. The content is solely the responsibility of the authors and does not necessarily represent the official views of Harvard Catalyst, Harvard University and its affiliated academic healthcare centers, or the National Institutes of Health. **Author contributions:** EBD, CEV, KM, WW, STR, PD, GPD and ETR designed the study. EBD, CEV, KM, WW, REL, JO'D, RB, AR, JH, STR, SER, EM, YF, RW, MM performed the experiments. EBD, CV, KM, WW, STR, REL, EM, JRS, YF, MM, GPD and ETR analyzed and reviewed the data. EBD, CEV, KM, STR, GPD and ETR wrote the manuscript. All authors reviewed and edited the manuscript. **Competing interests:** There is a patent pending on this work. **Data and materials availability:** All (other) data needed to evaluate the conclusions in the paper are present in the paper or the Supplementary Materials. Devices can be obtained through a material transfer agreement.

Figures

A)



B) OPTION A • NON POROUS • For Surface Modification



C) OPTION B • POROUS • For Therapy Delivery

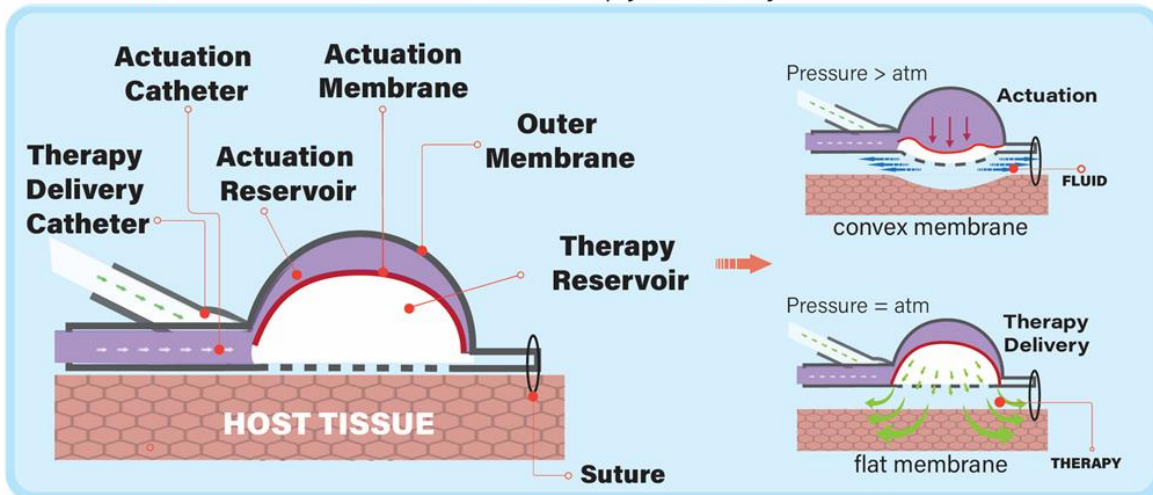
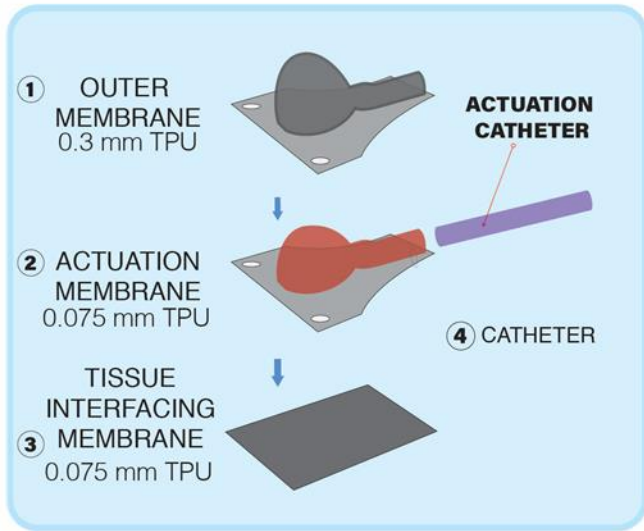
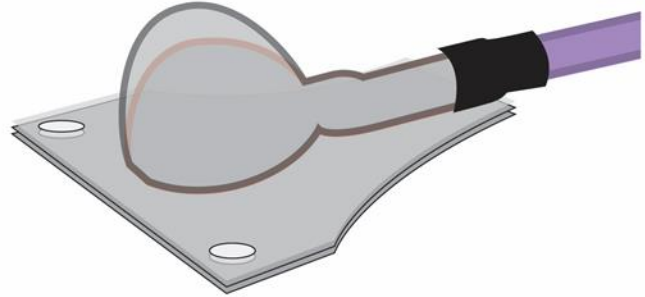


Figure 1: An overview of the device and the proposed mechanism of action. A) Implantable system showing a side-by-side implantation of a control and actuation group. B) Non-porous configuration of the DSR for foreign body modulation for implantable devices. C) Porous configuration of the DSR for therapy delivery.

A) **OPTION A** • **NON POROUS** • For Surface Modification

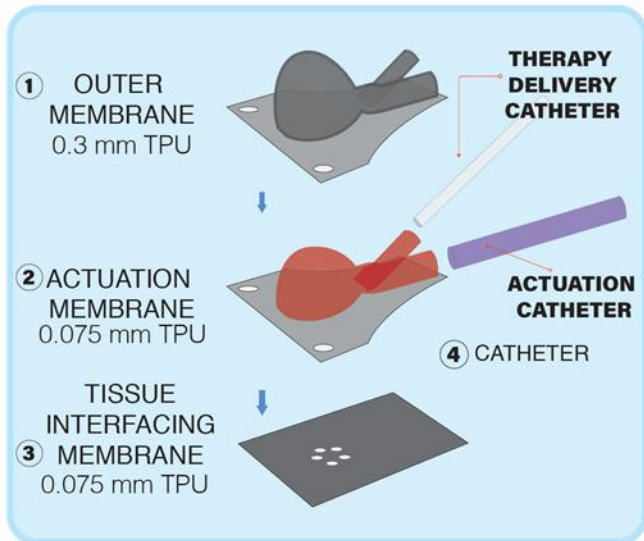


EXPLODED VIEW

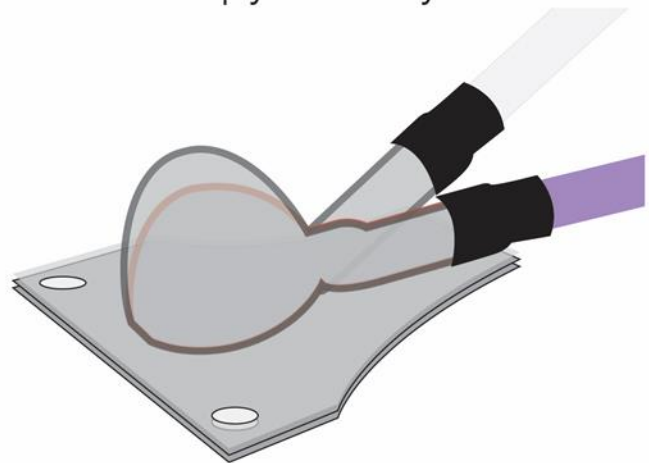


3D VIEW

B) **OPTION B** • **POROUS** • For Therapy Delivery



EXPLODED VIEW



3D VIEW

Figure 2: An overview of the configuration of the DSR devices A) Non-porous configuration for foreign body modulation for implantable devices. B) Porous configuration for therapy delivery.

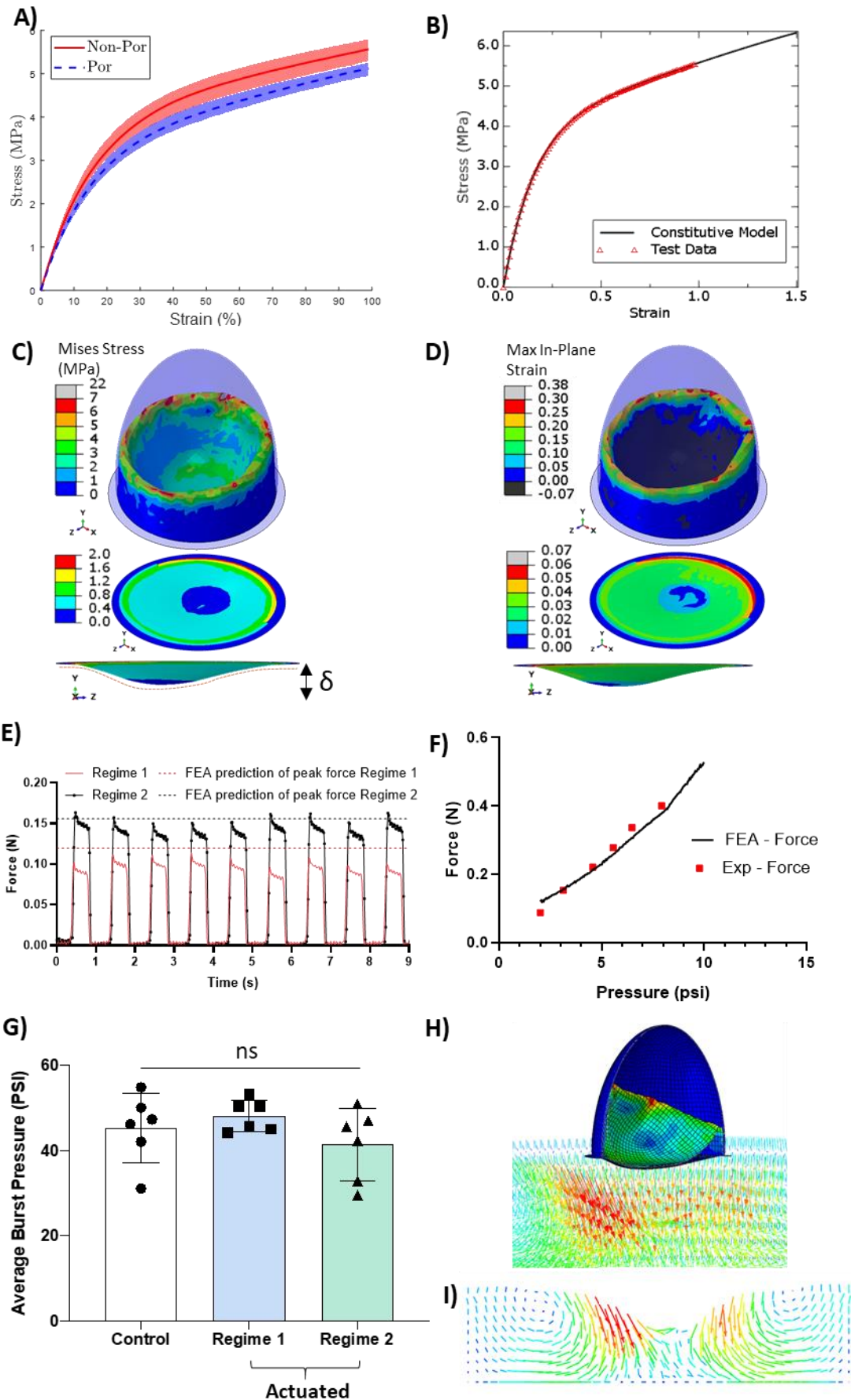


Figure 3: Computational and experimental characterization: A) Stress/strain plots for porous and non-porous thermoplastic urethane specimens. B) Fitting of the porous data to the Ogden

hyperelastic model. C) Mises stress contour plots for the overall device, and the lower membrane (top-down and side view where the broken red line illustrates deflection of the membrane). D) Maximum in-plane strain for the overall device, and the lower membrane (top-down and side view). E) Experimental cyclical force measurements two actuation regimes (regime 1 = 1 psi at 1 Hz, regime 2 = 2 psi at 1 Hz), and finite element predicted force for each. F) Relationship between input pressure and actuation force as measured experimentally, and predicted with finite element analysis (FEA). G) Burst failure of DSRs after actuating at regime 1 or regime 2 for 100,000 cycles. n=6/group, data are mean \pm SD p>0.05. H) 3D Smooth particle hydrodynamic model showing the direction and magnitude of fluid flow surrounding a DSR during actuation and I) 2D slice of model to illustrate direction and magnitude of fluid flow at the area of maximum deflection.

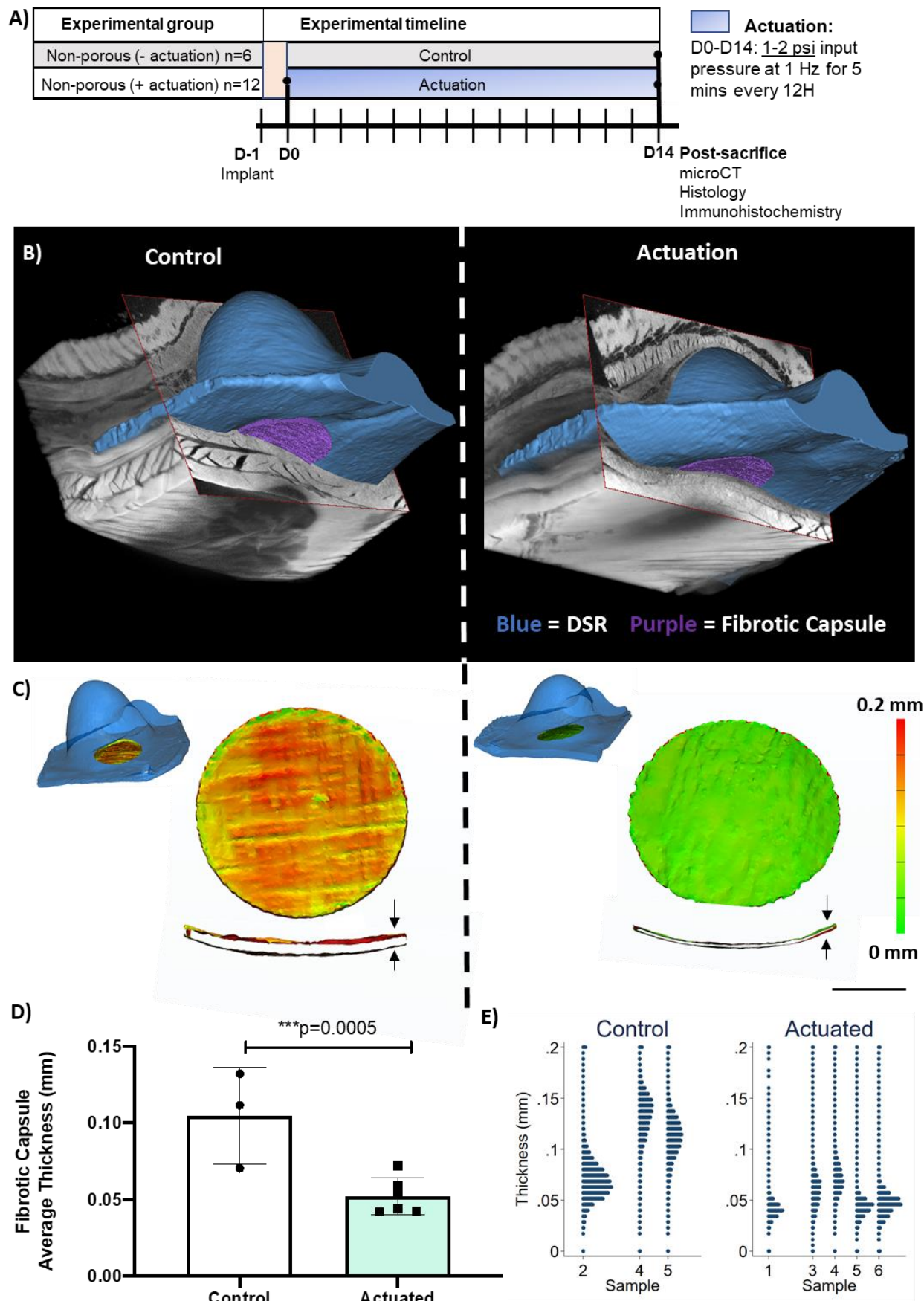


Figure 4: DSR reduces the fibrous capsule thickness *in vivo*. A) Timeline for *in vivo* studies for non-porous DSR. B) MIMICs reconstruction of soft tissue stained with PMA and imaged with microCT, where the DSR is shown in blue and the quantified segment of the fibrotic capsule is shown in purple. C) Thickness analysis in MIMICs where surface shell elements are shown, and

thickness is calculated as the distance between them. D) Average thickness across fibrotic capsule as measured by MIMICS. E) Dot plot of thickness measurement per sample (animal) $n=3-6/\text{group}$, data are mean \pm SD, *** $p<0.001$.

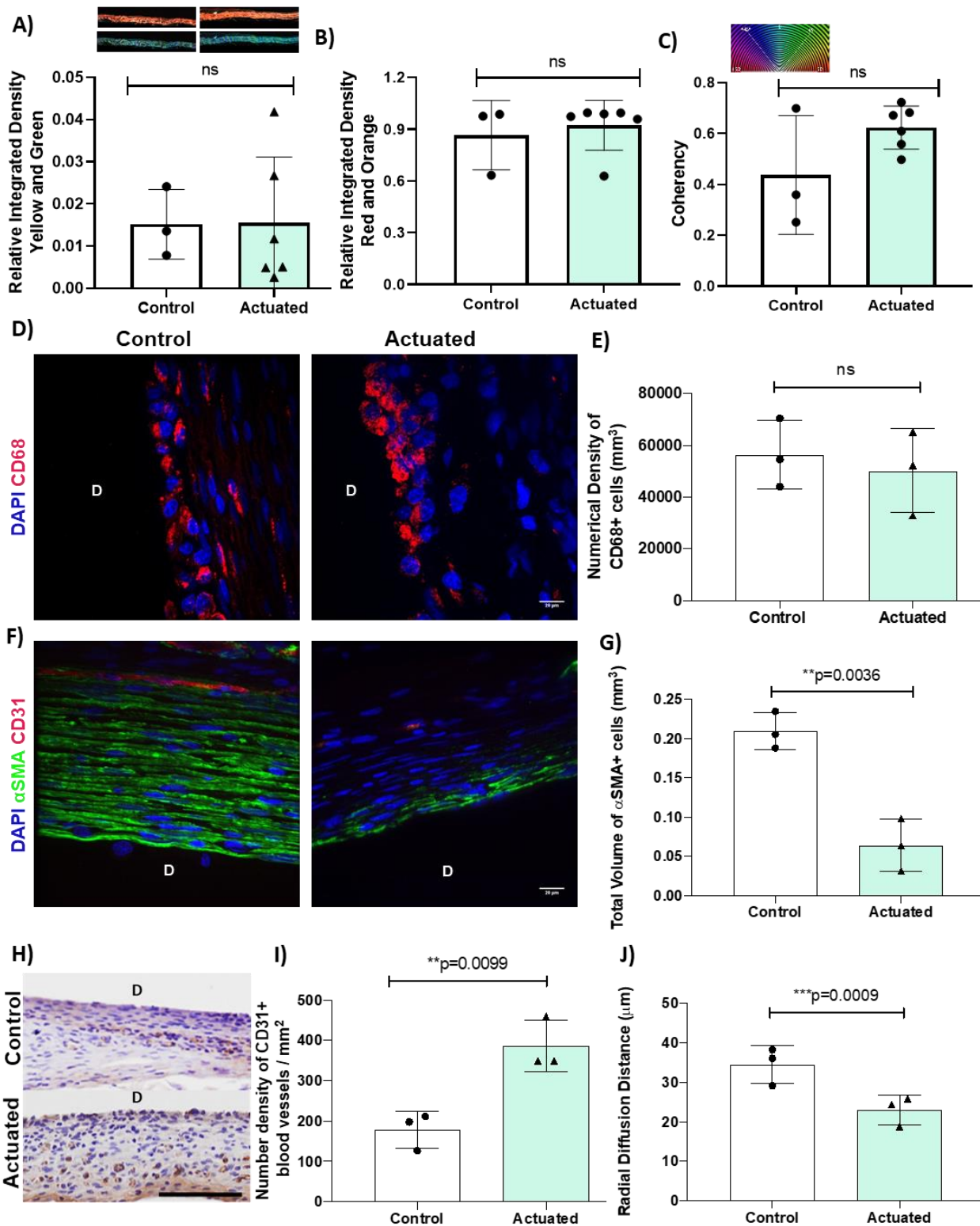


Figure 5: Histological analysis of the fibrous capsule. A) Relative integrated density of yellow and green fibers (signifying immature collagen) from polarized light microscopy images of the fibrous capsule in response to different treatments, with representative images shown. B) Relative integrated density of red and orange fibers (signifying mature collagen) from polarized light microscopy images of the fibrous capsule. C) Coherency of fibrous capsule based on polarized light microscopy. D) Representative immunofluorescent images of capsular tissue sections stained with

CD68 (Red = CD68, Blue = Hoechst). E) Numerical density of CD68 stained macrophages in different treatment groups. F) Representative immunofluorescent images of capsular tissue sections stained with α SMA (Blue = DAPI, Green = α SMA, Red = CD31). G) Total volume of α SMA+ cells (mm^3). H) Representative images of capsular tissue sections stained with CD31. I) Number of blood vessels/ mm^2 . J) Radial diffusion distance for regime 2 compared to control. D = device, n=3-6/group, Data are mean \pm SD, **p<0.01, ***p<0.001.

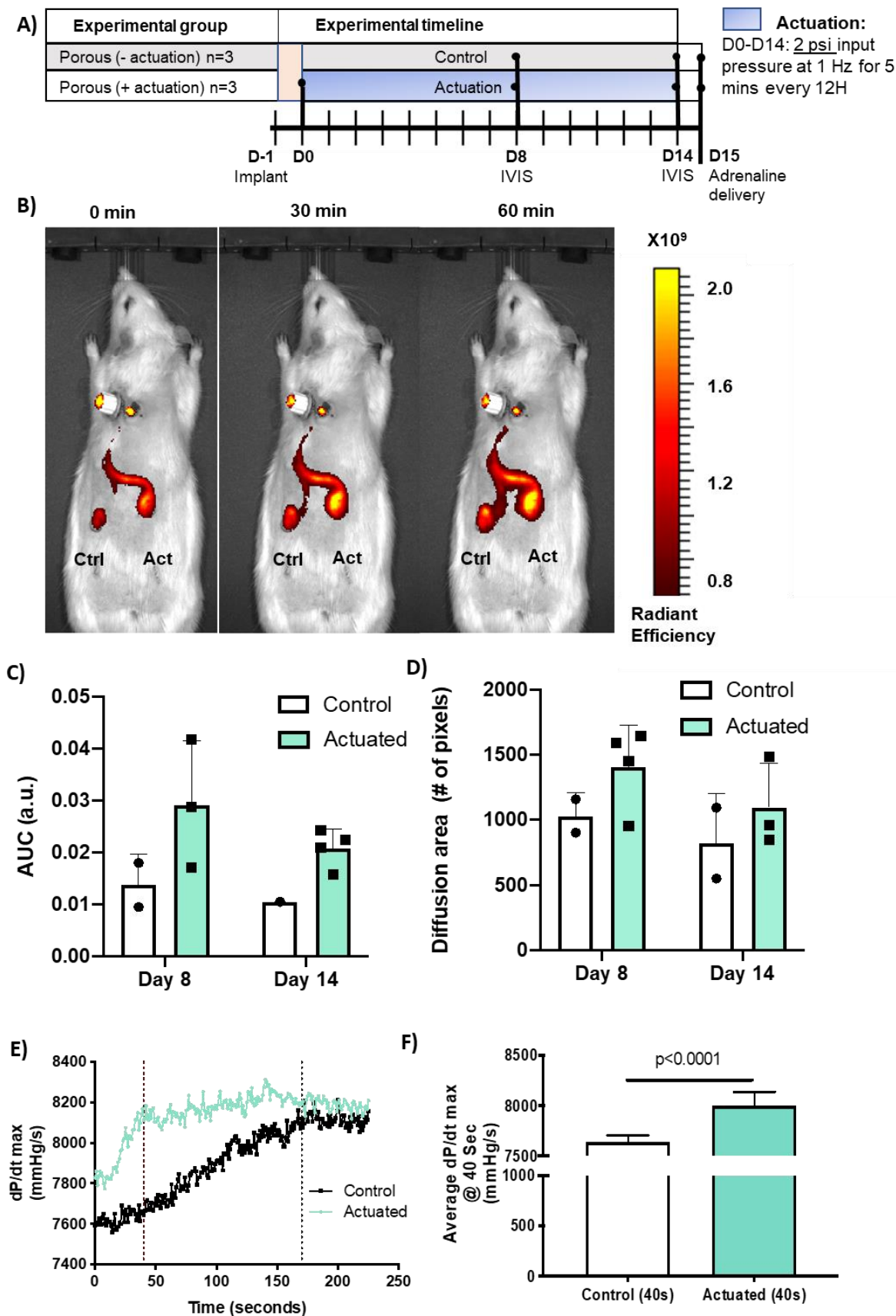


Figure 6: Enhanced pharmacokinetics through a porous DSR with actuation. A) Timeline for *in vivo* studies for porous DSR. B) Images from the *In Vivo* Imaging System (IVIS) at day 14 at 0 minutes, 30 minutes and 60 minutes showing the implanted actuation and control groups. C) Area under the fluorescence curve at day 8 and 14 for actuated and control groups n=2-4/group/timepoint, Data are mean \pm SD, *p<0.05. D) Diffusion area at day 8 and 14 for actuated and control groups

n=3-4/group/timepoint, Data are mean \pm SD. E) dP/dt max, a measure of ventricle contractility for the actuated and control DSRs in a representative animal. The vertical dashed lines show time to therapeutic effect for the control and actuated groups. F) Average dP/dT max per cycle for the first 40 seconds (the time to therapeutic effect for the actuated group). Ctrl=control, Act=act, AUC=area under the curve, a.u = arbitrary units.

SUPPLEMENTARY MATERIALS

Supplementary Materials and Methods

Applications of non-porous DSR arrays for modulating the FBR in indwelling medical devices

We propose that incorporating arrays of non-porous DSR arrays into medical devices that suffer from an adverse host response may offer a potential strategy to reduce these effects. We demonstrate physical embodiments of circular and linear arrays of DSRs, with reservoirs in series and in parallel, by encapsulating multiple reservoirs (manufactured from thermoplastic urethane or silicone - shown in color in Supplementary Fig. S2), and their actuation lines in a silicone sheet around a breast implant, and tubular structure that is ultimately envisioned for pacemaker leads or indwelling catheter lines (Supplementary Fig. S2).

Analytical model of the tissue-interfacing membrane

The strain field of the tissue-interfacing membrane was modeled as a clamped circular membrane with distributed pressure in the transverse direction. This is a well-known case in the field of shell theory and a variety of analytical approximations have been proposed (62). In this study, we used the analytical approximation of large deflection plate purposed by Zhang (62) to do a parametric study. All design parameters were identical to the lower membrane of the DSR except for the material model, which was assumed to be linear elastic with Young's modulus of 15 MPa and Poisson's ratio of 0.35. The effect of loading pressure (q), size (a), thickness (h), and material stiffness (E) of the membrane on the strain were evaluated. The details of this analytical approximation are based on the Von Kármán plate theory (63). The strain-displacement relations of an edge-clamped circular plate are given as follows;

$$\epsilon_r = \frac{N_r - \nu N_t}{Eh} = \frac{du}{dr} + \frac{1}{2} \left(\frac{dw}{dr} \right)^2 + \epsilon_o$$

Equation S1

$$\epsilon_t = \frac{N_t - \nu N_r}{Eh} = \frac{du}{dr} + \epsilon_o$$

Equation S2

where u , w are the displacement in the radial and tangential directions, a and h are the radius and thickness of the plate, and ϵ_o is the pre-stretch strain. As a clamped plate the deflection is assumed to be modeled by Equation S3 which satisfies the boundary conditions of a clamped plate, $w(0) = 0$ and $dw(0)/dr = 0$. The maximum deflection (w_0) and radial displacement (u) become Equation S4 and S5 deriving the principle of virtual work.

$$w = w_o \left(1 - \frac{r^2}{a^2} \right)$$

Equation S3

$$\frac{3}{4} \left(\frac{a^2}{h} \right) (1 + \nu) \epsilon_o w_o + \frac{1}{2} (1 + \nu) \frac{w_o^3}{h^2} = \frac{qa^4}{64D}$$

Equation S4

$$u = \frac{(5 - 3\nu)w_o^2}{6a^2} r + (\nu - 3) \frac{w_o^2}{a^4} r^3 + \frac{(10 - 2\nu)w_o^2}{3a^6} r^5 + \frac{(-7 + \nu)w_o^2}{6a^8} r^7$$

Equation S5

Using large-deflection circular plate analytical approximation, we predicted the deformation in the radial, vertical, and tangential directions along the radial distance, see Supplementary Fig. S6 To

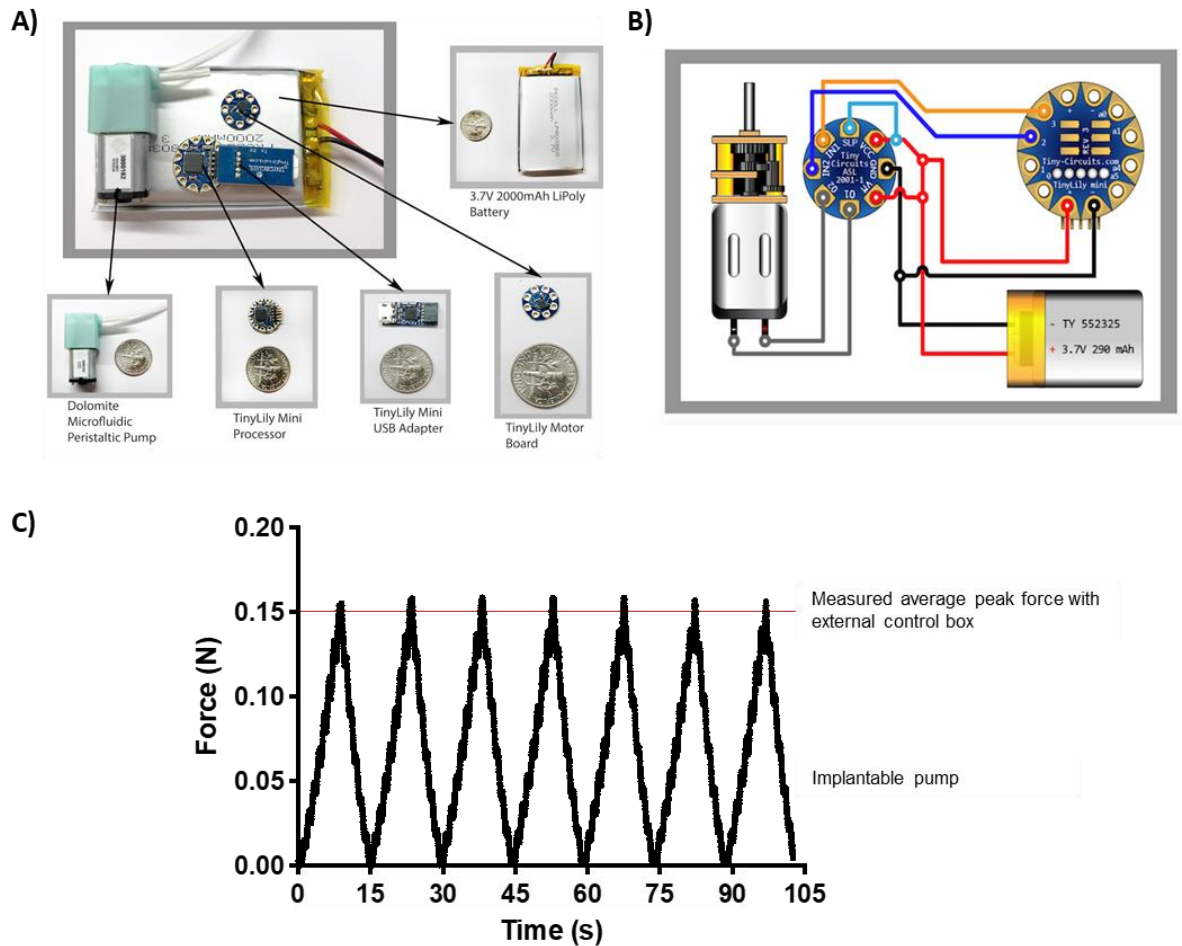
evaluate the performance of this approximation, w and r were nondimensionalized as $W = \frac{w}{h}$, $W_o = \frac{w_o}{h}$, and $\xi = \frac{r}{a}$

Where W_o is the deflection-thickness ratio, where $W_o < 0.05$ is usually considered small deflection, and $0.1 < W_o < 10$ is considered large deflection. The analytical approximation was compared with the numerical solution (FEA) using the W vs. ξ plots. Two scenarios were compared, shown in Supplementary Fig. S5a,b. The former was recreated from Zhang (62) with W_o of 0.95 and the latter was the lower membrane scenario with W_o of 6.1. They show that the approximation is more accurate with lower W_o . With the lower membrane scenario, the analytical approximation shows that the maximum deflection (0.46 mm) is located at the center while the maximum radial displacement (0.0013 mm) is not. According to Equation S1 and S2, the maximum radial strain (near the center), and maximum tangential strain (at the center) have similar magnitude (0.281%) but in different locations. The radial strain is largest in the central regions.

MIMICS segmentation and quantification of fibrous capsule thickness

Using MIMICS software (Materialise), dicom files were imported, opened and cropped between suture points on the device. A green mask was added to threshold the field of view. It was then cleared and edited using multiple slice editor to segment the fibrous capsule manually in the sagittal view. The fibrous capsule was mapped every five segments for the entirety of the CT dicom. The fibrous capsule was visually identified by a uniform change in signal intensity at the muscle border. After approximately fifty segments were mapped, interpolation was used to account for gaps between segments. Following completion of the green mask, an additional yellow mask was applied to the dicom to threshold the black and remove background. A boolean operator was applied (green mask-yellow mask) and subsequently created a third mask (cyan mask). The cyan mask was then edited using multiple slice editor using axial view to ensure consistency between different views. When the fibrous capsule was accurately complete in the cyan mask, it was edited in 3D. A circle (2.4 – 2.6 mm diameter) was cropped from the center of the fibrous capsule. A 3D file of this disc was exported as a .STL file for further analysis using 3-matic Research 10.0.0.212 software. The fix wizard was applied to the files, and a smoothing factor of 0.8 was applied. Auto-remesh was then applied. A wall thickness analysis was generated and the data was exported.

Supplementary Figures



Supplementary Figure S1: Implantable actuation system: A) Implantable components of the fully implantable pump B) Circuit drawing for the implantable pump. C) Force generation from the implantable pump compared to the average peak force measured by the custom-built external control box.

Circular Arrays



Model



Proof of Concept Prototype

Linear/Cylindrical Arrays



Model



Proof of Concept Prototype

Device Application

- Breast Implants -



Clinical Problem

- Capsular Contracture

Device Application

- Implantable Pacemaker Leads -



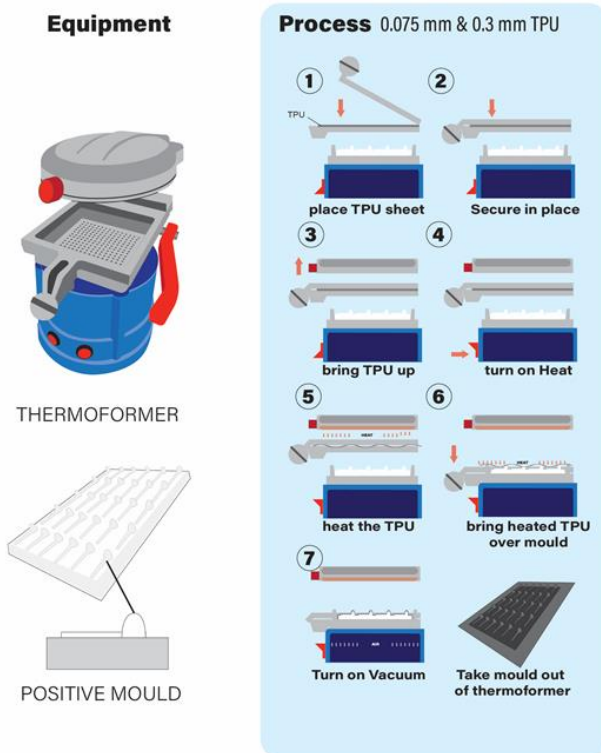
Clinical Problem

- Fibrosis at tip

Supplementary Figure S2: Non porous DSR arrays to reduce complications associated with implantable devices. Circular arrays are encapsulated around a breast implant, and a linear array is integrated into a cylindrical structure, ultimately envisioned for pacemaker leads. DSR arrays are shown in color, with each color representing an individual actuation line.

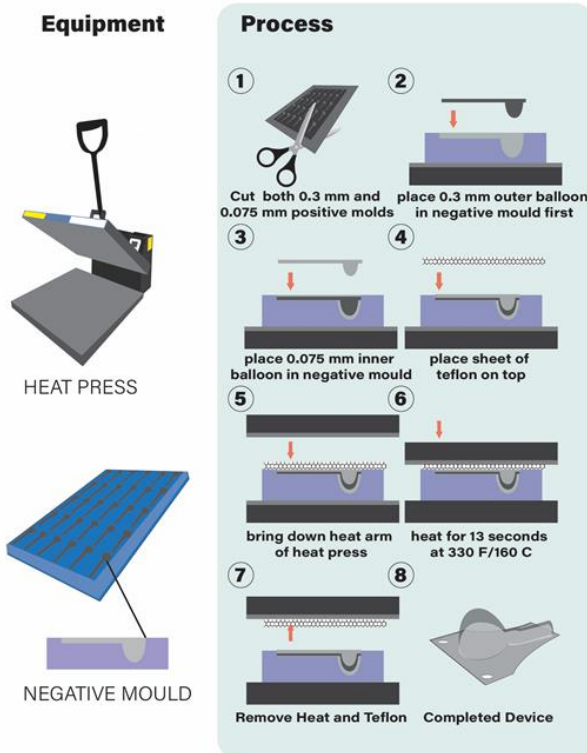
A)

THERMOFORMING

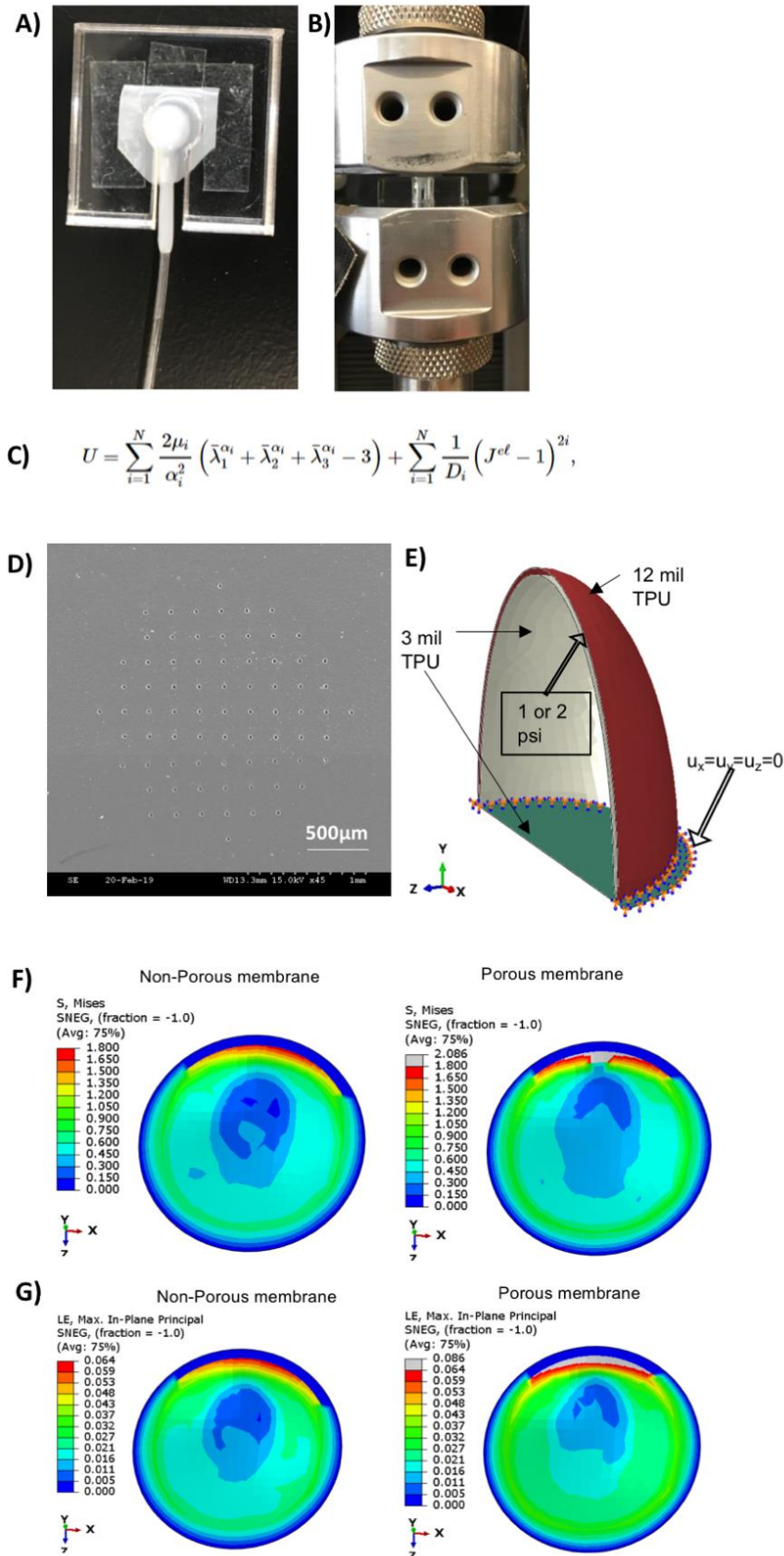


B)

HEAT SEALING

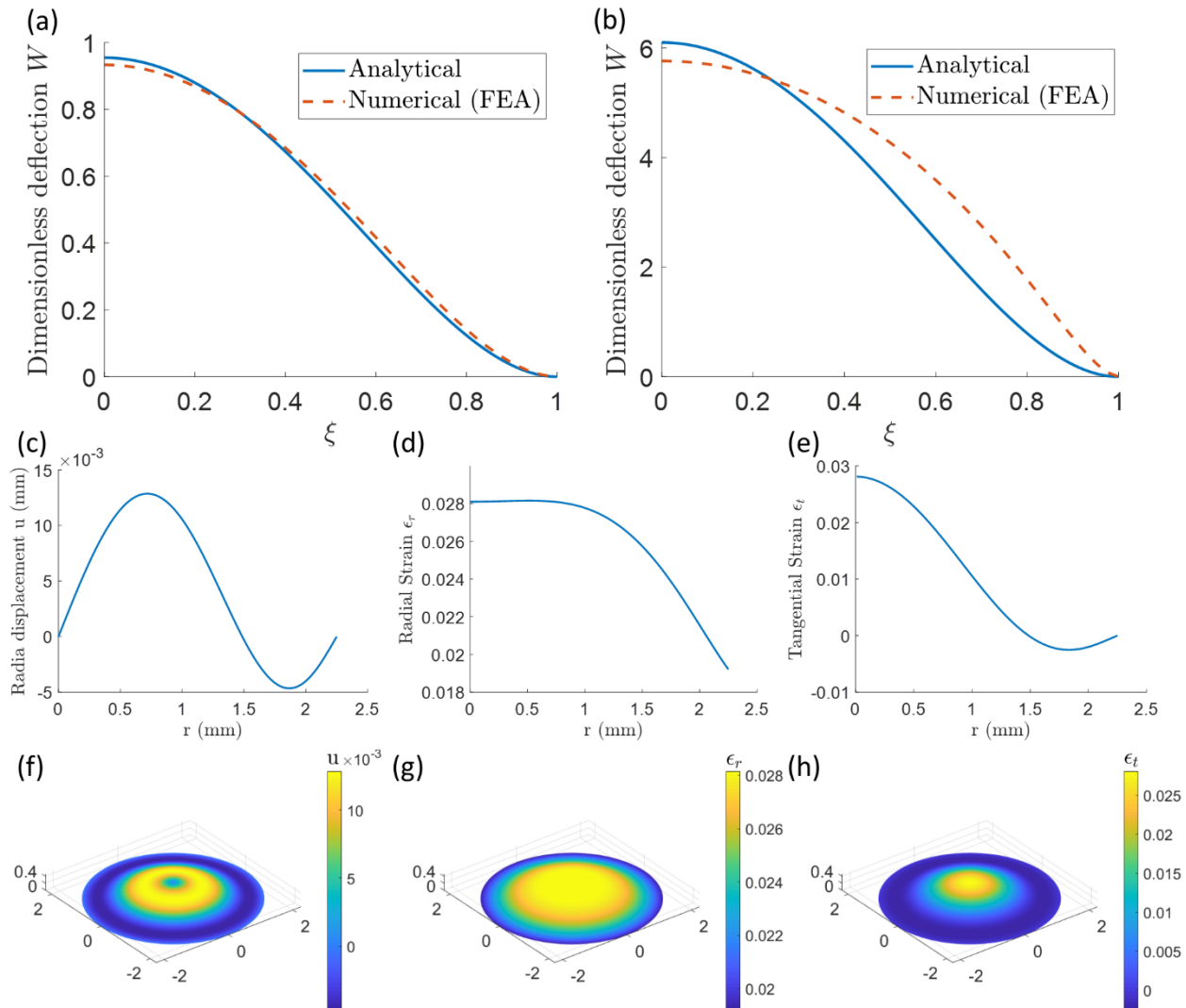


Supplementary Figure S3: Device manufacture procedure which involves two step – thermoforming and heat sealing. **A) Thermoforming:** 1) Thermoplastic urethane (TPU) sheets (0.075 mm and 0.3 mm) were mounted separately in a thermal former with a vacuum platform and a positive 3D printed mold was placed on the platform, 2) The TPU sheet was secured in place, 3) The TPU was brought close to the heating element, 4) the heat was turned on, 5) the TPU was heated until it sags in the center, 6) the platform was lowered over the positive mold, 6) the vacuum was applied to form the sheet over the positive mold, 8) the formed TPU was removed from the positive mold. **B) Heat sealing:** 1) The formed TPU was cut out, 2) 0.3 mm TPU was placed in a 3D printed negative mold, 3) 0.075 mm TPU was placed in a 3D printed negative mold on top of the 0.3 mm mil TPU, 4) A teflon strip was inserted into the groove of the negative mold between relevant layers of TPU to keep the catheter channels open during the following heat-sealing 5) a 0.075 mm TPU membrane (porous or non-porous) was placed on top and a layer of Teflon was played on top to protect the assembly, 5) the arm of the heat press was brought down on top of the mold, 6) the assembly was heat sealed with a heat transfer machine, 7) the heat arm and Teflon was removed, 8) device reservoir was complete. Catheter tubing was inserted into relevant channels and heat shrink tubing was used to seal the devices.

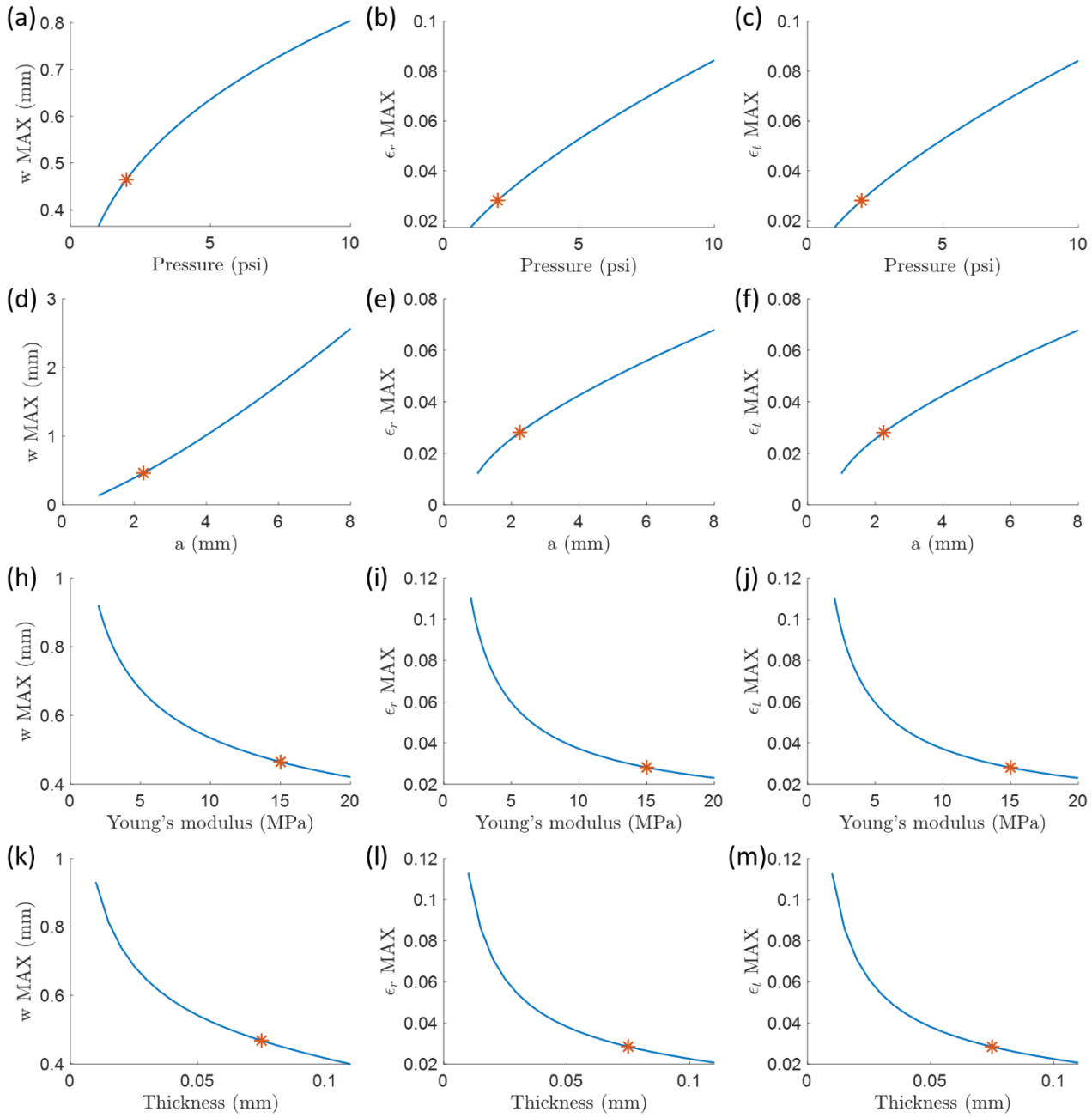


Supplementary Figure S4: Test set-up for force characterization and porous vs non-porous computational models. A) Acrylic holder for supporting reservoir and ensuring that lower functional membrane is in contact with upper cross-head. B) Test set-up in mechanical tester. C) Strain energy density function for Ogden model. D) Light microscopy of laser-cut porous membrane. Pore diameters were 10 micron with spacing of 200 microns. E) Boundary conditions

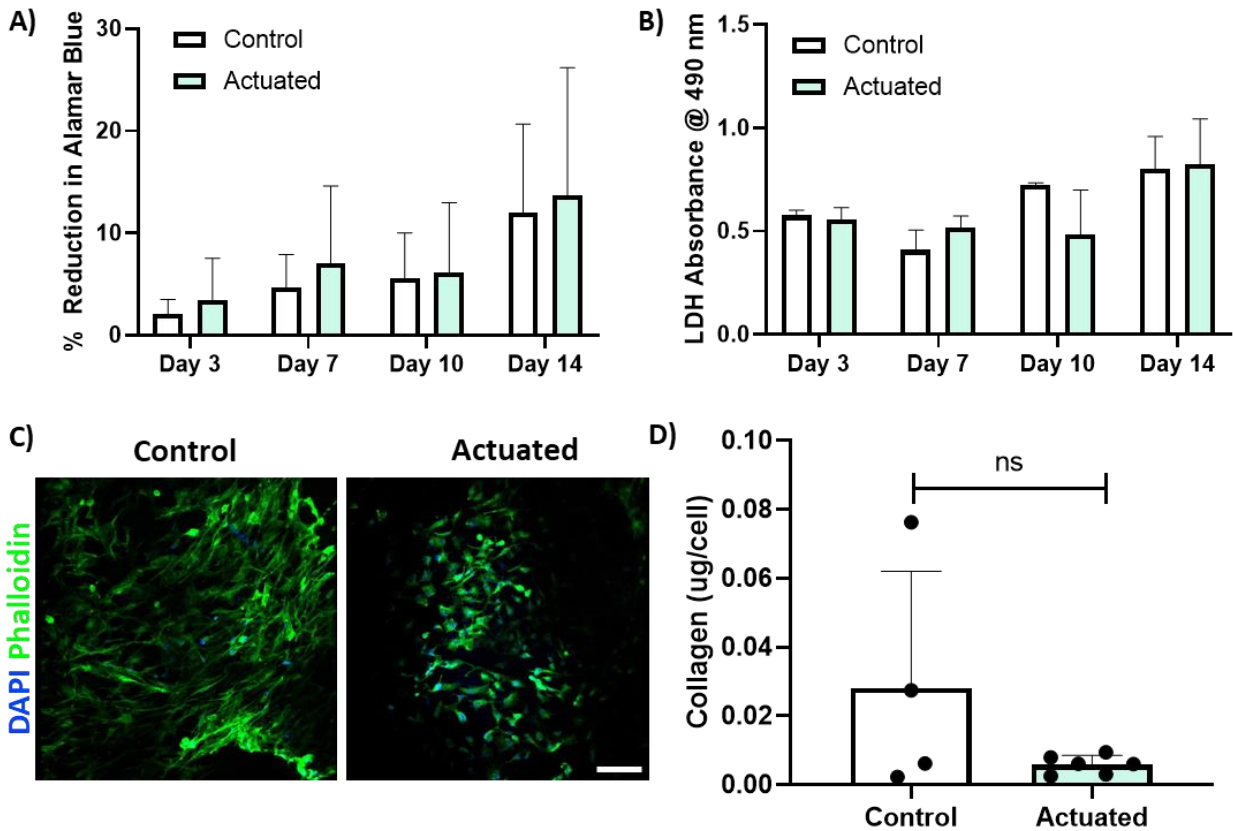
applied to the finite element model. F) In-plane strain and G) Mises stress for the porous vs non-porous DSRs showing relatively small differences.



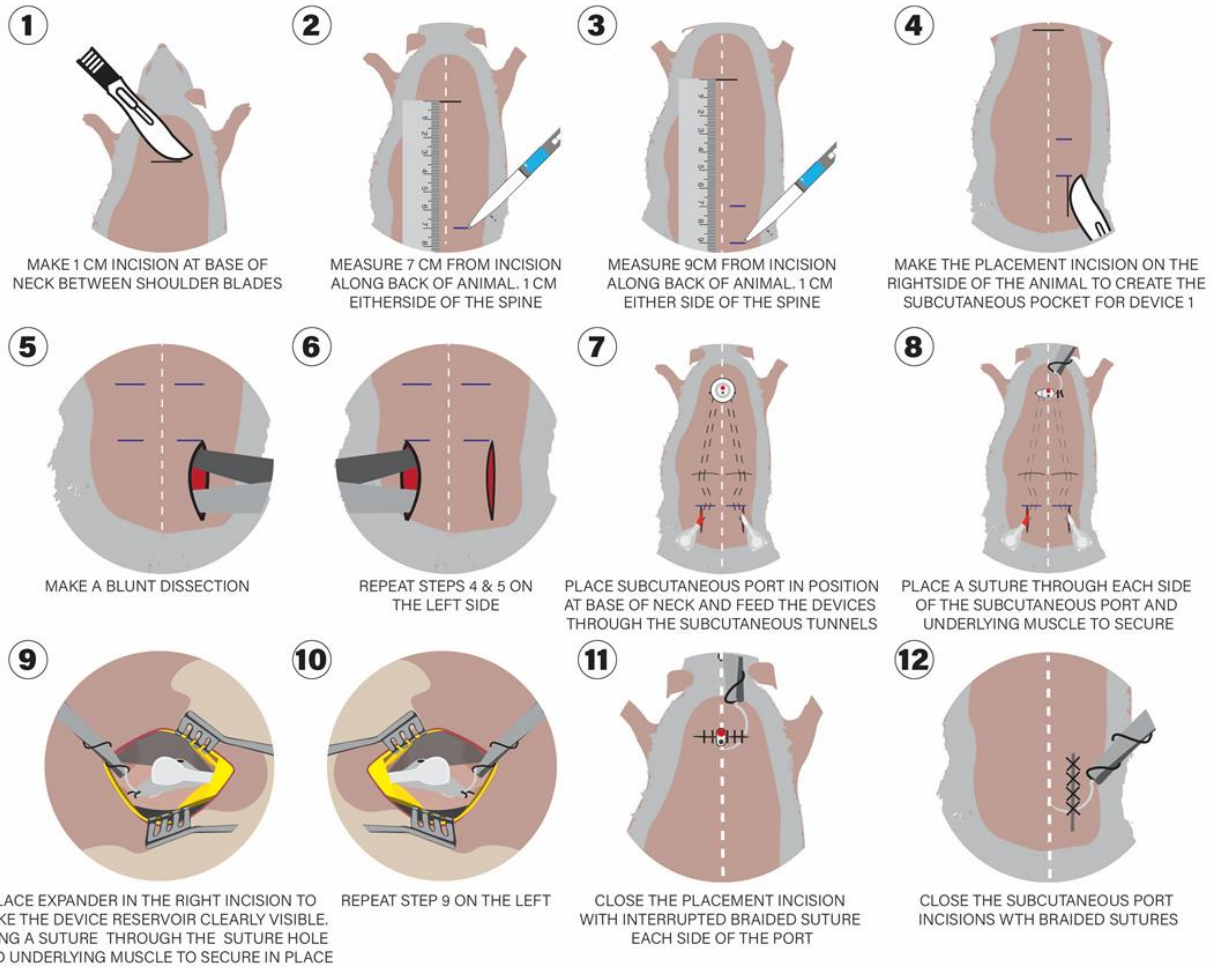
Supplementary Figure S5: Analytical approximation for large deflection circular plate. (a, b) Plots of dimensionless deflection (w) along with dimensionless radius (ξ) to compare the analytical and numerical solutions. The plate parameters a , h , E , q are recreated from Zhang [27] in (a) and are have the same dimensions as the lower membrane of the DSR in (b). (c - e) Plots of radial displacement (u), radial strain (ϵ_r), and tangential strain (ϵ_t) along with radial distance (r) under the lower membrane condition. (f - e) The corresponding counter plots of u , ϵ_r , and ϵ_t .



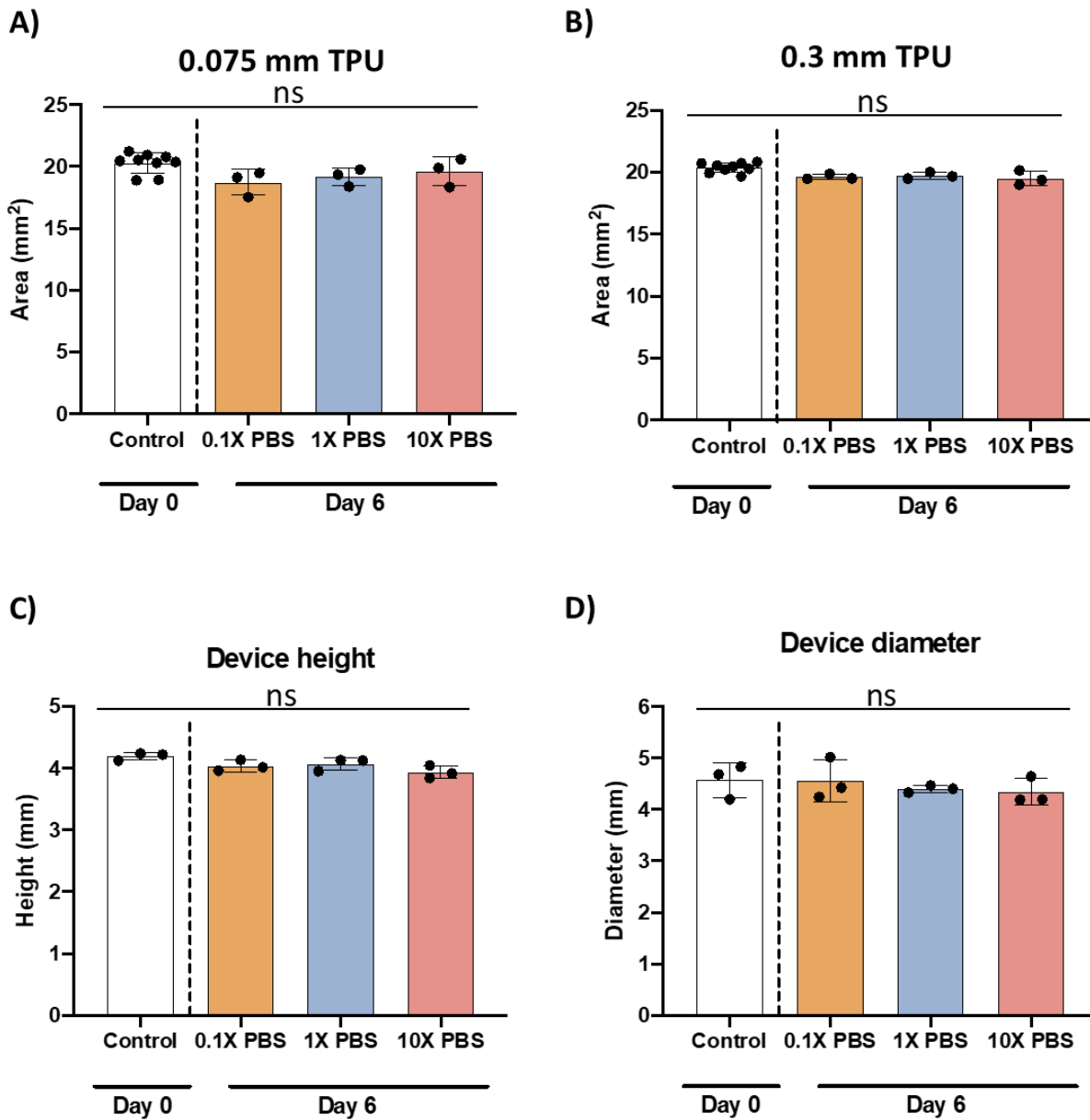
Supplementary Figure S6: Parametric study using large deflection plate analytical approximation. Using the lower membrane scenario (orange star) as the baseline, pressure (a-c), size (d-f), material stiffness (h-j), and membrane thickness (k-m) are tuned showing the effects on w , ϵ_r , and ϵ_t .



Supplementary Figure S7: *In vitro* assessment of the effect of actuation of non-porous DSR on myofibroblasts cell line (WPMY-1). A) Metabolic activity as shown by % reduction in alamar blue, B) Cell viability as shown by LDH absorbance at 490 nm, C) Representative immunofluorescent images of WPMY-1 cells on the tissue-interacting membrane of the non-porous DSR with stained actin cytoskeleton and nuclei (Blue = DAPI, Green = phalloidin), scale bar = 100 μ m, D) Cumulative soluble collagen production per cell for actuated compared to non-actuated control DSR. Data are mean +SD, n=4-8/group.



Supplementary Figure S8: Pre-clinical implementation of the DSRs. A) Device implantation procedure. Each animal has two implanted DSR devices subjected to no actuation, regime 1 or regime 2.



Supplementary Figure S9: The dimensional effects of submerging the device, and its constituent material in saline with different concentrations. A,B) the area of thermoplastic urethane (TPU) specimens before and after soaking in PBS of various concentrations for 6 days. (C,D). The height and diameter of the DSR at day 0 and after 6 days submerged in PBS of various concentrations. No significant dimensional changes were observed.

Supplementary Movie S1: Actuation of DSR with implantable pump.

A side view and top-down view of DSR being actuated with an implantable pump are shown.

Supplementary Movie S2: Actuation of low profile non-porous DSR.

A side view and top-down view of a low profile DSR being actuated.

Supplementary Movie S3: Actuation of DSR in vivo.

The actuation of the subcutaneous DSR in the rat model is shown.